Rock Mechanics and Rock Engineering (2020) 53:5715–5744
https://doi.org/10.1007/s00603-020-02238-5

ORIGINAL PAPER

Can Heating Induce Borehole Closure?

Xiyang Xie[1] · Andreas Bauer[3] · Jørn F. Stenebråten[1] · Sigurd Bakheim[1] · Alexandre Lavrov[1] · Erling Fjær[1,2] · Tron G. Kristiansen[3]

Received: 19 August 2019 / Accepted: 25 August 2020 / Published online: 12 September 2020
© The Author(s) 2020

Abstract

The current study shows that heating a cased borehole in low-permeability shale rock can induce plastic deformation, leading to the closure of the casing annulus and decreasing annulus connectivity. The thermally induced borehole closure is interesting for the field operation of plug and abandonment (P&A), as it potentially saves operation cost and time by avoiding cutting casing and cementing. Lab experiments and numerical simulations are implemented to investigate the thermally induced borehole closure. Pierre shale and a field shale are tested. The lab experiments are performed by heating the borehole wall in a 10-cm-OD hollow cylinder specimen. Here, a novel experimental setup is applied, allowing for measuring temperature and pore pressure at different radii inside the specimen. Both the experimental data and the post-test CT images of the rock samples indicate the rock failure by borehole heating, and under certain conditions, heating results in an annulus closure. The decrease of hydraulic conductivity through the casing annulus is observed, but this decrease is not enough to form the hydraulic-sealed annulus barrier, based on the results obtained so far. Lab-scale finite-element simulations aim to match the lab results to obtain poro-elastoplastic parameters. Then the field-scale simulations assess the formation of shale barriers by heating in field scenarios. Overall, (i) the lab experiments show that heating a borehole can increase the pore pressure in shale and hence induce rock failure; (ii) the numerical simulations match the experimental results reasonably well and indicate that the heating-induced borehole closure can sufficiently seal the casing annulus in the field-scale simulation.

Keywords Rock failure · Borehole closure · Plug and abandonment (P&A) · Thermal pressurization · Thermo-poro-elastoplasticity · Shale rock

1 Introduction

In petroleum engineering, plug and abandonment (P&A), as the last operation of a well, aims to isolate the wellbore permanently. Unsuccessful implementation of P&A may cause fluid leakage, which may escalate to an environmental crisis without proper countermeasures. A traditional P&A is challenging for its capital intensity and time consumption since the casing is to be cut and pulled and the cement plug is to be set across the borehole as a permanent barrier. Cement bond logging (CBL) indicates that the deformation of soft rock, shale or mudstone, can form a permanent barrier and isolate casing annulus hydraulically (Williams et al. 2009). If an effective barrier exists in the casing annulus, the P&A standard, for example, NORSOK D-010 (Norsok 2013), only requires setting a cement plug inside the casing without cutting and pulling, which can save operation cost and time. This study aims to reveal whether heating a cased borehole can induce such an effective barrier in the casing annulus.

Thermal pressurization is the major mechanism that has the potential to induce failure in low-permeability shale in saturated condition: thermally induced pore pressure can be built up inside rock due to larger thermal expansion of pore fluid than that of rock frame and faster thermal diffusion than pore pressure diffusion (Campanella and Mitchell 1968; Ghabezloo and Sulem 2009). The intensity of thermally induced pore pressure can be quantified as the thermal pressurization coefficient defined as the pore pressure increment per unit temperature increment (Ghabezloo and Sulem 2009, 2010). The coefficient mainly depends on the nature of the material, the state of stress, the range of temperature

✉ Xiyang Xie
xiyang.xie@sintef.no; xiyang.xie.1989@gmail.com

1 SINTEF Industry, Trondheim, Norway

2 Norwegian University of Science and Technology, Trondheim, Norway

3 Aker BP, Trondheim, Norway

change, and the induced damage (Ghabezloo and Sulem 2009). As a result of thermal pressurization, the effective stress applied to the rock frame is decreased and the rock can exhibit shear or tensile failure. As shown in Fig. 1, the Mohr circle shifts to the left due to the decrease of effective stress. By increasing the temperature in the formation around the borehole, the rock can expand along the radial direction but it is restricted to expand in the tangential direction (the direction perpendicular to the radial one and in the same plane perpendicular to the borehole axis). As a result, the thermal strain is built up along the radial direction and thermal stress is built up in the tangential direction. The thermal stress contributes additionally to the total stress in the tangential direction and will increase the shear stress around the borehole. The increased shear stress can assist in rock yield and thus contribute to borehole closure. As shown in Fig. 1, the Mohr circle is enlarged while it is shifting to the left due to borehole heating. In this study, thermal stress is regarded as a minor mechanism. Creep of the rock frame is not discussed here.

Circulating mud through the cased borehole or injecting fluid into the reservoir can vary the temperature field around the borehole. This has an impact on the borehole stability (Stephens and Voight 1982; Wang et al. 1996; Chen and Ewy 2005; Hou and Luo 2011; Yan et al. 2014; Kanfar et al. 2015; Gao et al. 2017). For example, as the temperature increases at the borehole wall, both fracture pressure and collapse pressure will rise (Yan et al. 2014). The heated fluid can cause the effect of thermal pressurization and thermal stress buildup as explained previously. The cooled fluid inside the borehole may decrease thermal stress. In an extreme case, the effective stress may convert to a tensile state even without pressurization of pore fluid (Yao et al. 2017).

Heating inside the borehole results in heat diffusion around the borehole. The thermal stress arises in the heated rock matrix, which leads to an increase in effective stress. Meanwhile, the pore pressure increases due to the thermal pressurization, which results in a decrease of the effective stress. Thermal stress and thermal pressurization can be quantified by the thermal expansion coefficient of the rock matrix and the fluid (see Table 1). Since (i) the formation fluid has a significantly higher thermal expansion coefficient than that of the rock matrix, (ii) the formation is constrained by the in-situ stress, and (iii) the permeability of shale is in the nano-Darcy range (faster heat diffusion than hydraulic diffusion or nearly undrained condition), the overall contributions of the above three factors imply a decrease of effective stress (see Fig. 1). The thermally induced pore-pressure increase for this material exceeds 0.1 MPa/ °C (Chen and Ewy 2005; Bauer et al. 2017). Based on the Mohr–Coulomb yield criterion, reduction of the effective stress can yield rock failure. Shear failure may occur with sufficient shear stress (for example due to the stress concentration around the borehole). Tensile failure may happen if shear stress is small enough and the minimum effective principal stress violates the tensile strength (see the illustration in Fig. 1).

After thermoelasticity and poroelasticity has been introduced by Biot's work (1941, 1955, 1956), many pieces of

Table 1 Volumetric thermal expansion coefficients of several minerals and water at room temperature

Mineral	Volumetric thermal expansion coefficient (10^{-5}/ °C)
Abyssal Red Clay	3.4 (McTigue 1986)
Salt in Salado Formation	1.2 (McTigue 1986)
Quartz	3.3 (Walsh 1973)
Water at 20 °C	25.2 (Sharqawy et al. 2010; Nayar et al. 2016)

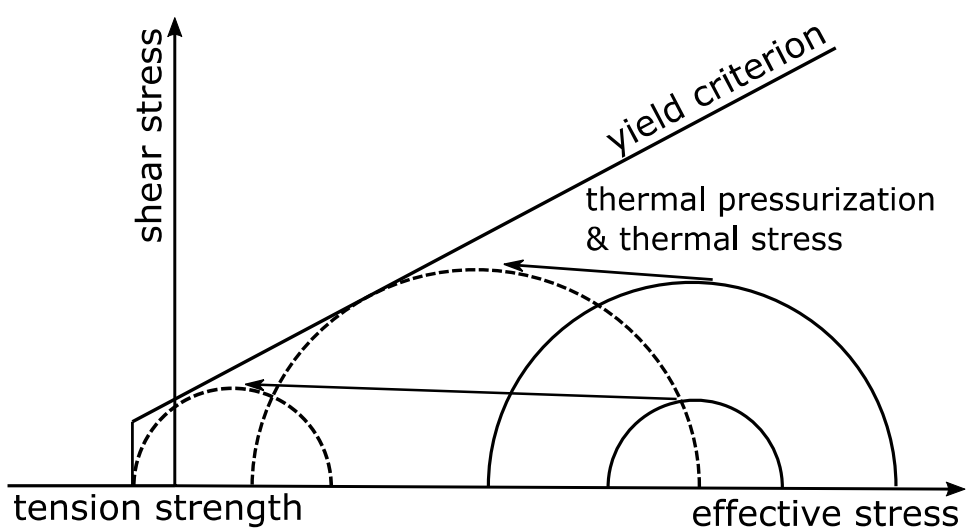

Fig. 1 Rock failure due to the pore pressure increase

research have been developed afterward; some are highlighted here (for comprehensive reviews see, for example, Li 1998 and Uribe-Patiño et al. 2017). Biot's work has been extended by several authors to the thermo-pore-elasticity (Rice and Cleary 1976; Bear and Corapcioglu 1981; Palciauskas and Domenico 1982; Detournay and Cheng 1988; Kurashige 1989; McTigue 1990; Coussy 1995; Cui et al. 1997). Rice and Cleary (1976) reformulated Biot's model of poroelasticity. Kurashige (1989) extended Rice and Cleary's formulation to non-isothermal conditions with different thermal expansion coefficients for pore fluid and solid frame. McTigue (1990) formulated the exact solution of thermally induced fluid flow around a borehole under plane strain and axisymmetric conditions.

Some researchers consider more complicated scenarios around the borehole. Detournay and Cheng (1988) obtained the fully coupled solution of stress, pore pressure, and displacement of a vertical borehole surrounded by a non-hydrostatic stress field. Wang and Papamichos (1994) formulated the transient analytical solution around a circular borehole subjected to a quick change of temperature and wellbore pressure. Cui et al. (1997) and Li (1998) derived the poroelastic solution for an inclined borehole. Abousleiman and Ekbote (2005) formulated the analytical thermo-poroelastic solution for the inclined borehole in a transversely isotropic medium subjected to an arbitrary stress state.

The research of poroelasticity was also developed in another direction: the behavior of saturated rock after failure. Rice (1975) formulated a plastic stress–strain relation with dilatant hardening of the saturated rock mass. Coussy (1989) introduced the general theory of thermo-poro-elastoplasticity of the saturated porous material by considering the plastic porosity. Hueckel and Borsetto (1990) formulated the constitutive equations of the thermo-elastoplasticity of shale due to heating, which considered the effects of thermal softening and plastic-hardening. Wang and Dusseault (1995) analyzed the thermally induced failure in the low-permeability medium around the borehole, which implies that borehole heating can enlarge the plastic zone and vice versa. Bauer et al. (2017, 2019) simulated borehole closure with rock failure around the borehole by heating the borehole wall.

Either convection or conduction can dominate heat transfer inside a porous medium (e.g. Kurashige 1989; Kanfar et al. 2016). Hou and Luo (2011) and Hojka and Dusseault (1990) reported that the conduction governs the heat flow in porous media when the permeability is smaller than 10^{-15}–10^{-14} m^2. The permeability of shale in this study is as low as 10^{-17} m^2, so we expect that conduction can be in charge of the heat transfer.

The thermal effects on claystone and shale have been investigated. Johnston (1987) revealed the physical properties of the North Sea Malm shale samples at different temperatures and pressures and observed that elevated temperature can induce more irreversible deformation at the same confining pressure. Similar thermal properties of Opalinus shale were found by Favero (2017). Bauer et al. (2017) also observed similar behavior in a field-shale with the stepwise increase of temperature at constant deviatoric stress. Zeuch (1983) found that the strength of the Anvil Points shale (an oil shale) is inversely proportional to the temperature. Mohajerani et al. (2013) developed an apparatus to investigate the thermal pressurization of claystone. The results indicate that the thermal pressurization coefficient is temperature-dependent. Yu et al. (2014) concluded a series of field experiments about the thermally induced damage zone around a repository for nuclear waste disposal, which implies that thermally induced plasticity, swelling, and creep are beneficial to seal fractures around the borehole and to maintain low permeability of the rock barrier.

Very few papers reported experimental devices that can test specimen with hollow cylinder geometry with the influence of temperature. Salisbury et al. (1991) proposed an apparatus testing borehole instability of the hollow cylinder specimen with pore pressure control and mud circulation control inside the borehole. The apparatus had the ability to control the mud temperature, but the tests focused on the chemical properties of mud, which induced swelling and hydration of the smectite shales. Delage (2013) studied the thermal impact with a hollow cylinder triaxial apparatus by applying the same confining pressure on the inner and the outer lateral surface of the hollow cylindrical specimen and the controllable ambient temperature. So far, we have not been aware of any laboratory apparatus with a hollow cylindrical specimen, which can control the ambient temperature and borehole temperature independently and measure the temperature and pore pressure inside the rock directly.

The hollow cylinder apparatus introduced in this paper provides the possibility to control temperatures at the borehole and at the outer lateral surface independently and to monitor temperature and pore pressure at different radial positions inside the hollow cylinder specimen.

ABAQUS, a finite-element software, is utilized in the numerical part of this study. The constitutive behavior of the rock is poroelastic coupled with heat conduction and enframed by the Mohr–Coulomb yield criterion and tensile failure (Dassault Systèmes 2014). Note that the Biot coefficient is not explicitly defined as one of the simulation input but internally computed based on other assigned rock properties (Haug 2019; Haddad and Eichhubl 2020). This software is first used to simulate the lab-scale hollow cylinder tests. The simulations aim to match the experimental results. The material properties obtained in the lab-scale simulation are applied to a field-scale geometry to assess the potential of forming a shale barrier by heating the borehole in the field condition.

This paper is organized as follows. Section 2 describes the novel experimental setup. Section 3 summarizes the experimental results. Section 4 shows the lab-scale and field-scale simulations. Section 5 discusses several issues about lab tests and simulations.

2 Experimental Setup

Borehole heating tests were performed in a hydrostatic compaction cell with 10-cm-diameter hollow-cylinder specimens of two types of shales. As shown in Fig. 2, a novel experimental setup was developed, allowing for measuring temperature and pore pressures at different radial positions inside the shale (at 16.25 mm, 27.50 mm, and 38.75 mm from the borehole axis). In order to probe pore pressure and temperature inside the specimens during heating, small holes (1.7 mm diameter) were drilled into the specimen: three holes in the vertical direction (parallel to the borehole axis) at three different radial positions, and three holes in the radial direction (normal to the borehole axis) from the outside of the specimen at mid-height with depths corresponding to the radial positions of the pore-pressure sensors (Fig. 2a, c).

Steel capillary tubes connected to pore-pressure transducers were inserted through the bottom endcap into the vertical holes that reach up to the mid-height of the specimen (see Fig. 2d). The total dead volume of each pressure sensor was less than 0.1 ml, which is sufficiently small for pressure measurements in a low-permeability shale, as confirmed by Skempton-B test measurements (larger dead volumes would result in delayed pressure responses and pressure readings that would be smaller than the actual pressure). The Skempton-B test was performed on an additional Pierre shale with hollow cylindrical geometry. The sample was stabilized at confining pressure 9 MPa and pore pressure 6 MPa. The confining pressure was then increased by 1 MPa for 15 min and was held constant for 1 h, then it was reduced to 9 MPa again. The pore pressure response at the outermost position had an increment of 0.8 MPa. The pore pressure increment was somewhat delayed relative to the confining pressure increment, which may be ascribed to the low permeability around the hole of the sensor. The trend of pore pressure time-evolution showed a persistent increase when the confining pressure was held constant, and it is likely that the pore pressure response would be significantly higher than 0.8 MPa if the confining pressure was held longer at this elevated level.

A picture of a mounted specimen is shown in Fig. 2b. Thermocouples were inserted into the radial holes. To prevent heat convection inside the holes that could have an impact on the temperature probed by the thermocouples, the thin thermocouple wires were fed through PEEK capillary tubes that were inserted into the radial holes. The

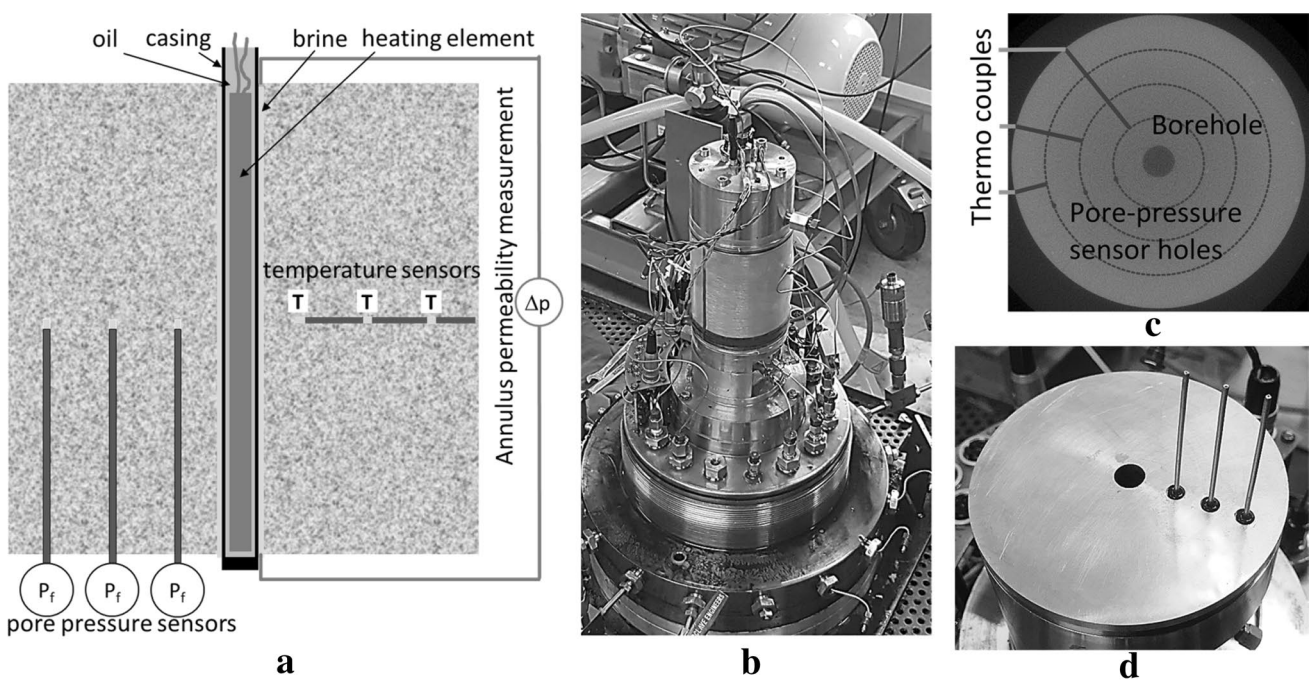

Fig. 2 **a** Illustration of the cross-section of the specimen with sensors. **b** Picture of a mounted cylinder specimen. **c** CT image of a cross-section of the specimen illustrating the borehole, the small holes for the pore-pressure sensors, and the radial holes for the temperature sensors drawn schematically. **d** The lower endcap with the O-ring sealed capillary tubes that are inserted into the specimen for pore-pressure measurements

thermocouple wires were fed out underneath the sleeve by which the specimen was sealed against the confining oil. To this end, one of the O-rings between the sleeve and endcap was replaced by two layers of vulcanizing tape in between which the thermocouple wires are fed through. For pore-pressure control on the outside of the specimen, a metal mesh is wrapped around the specimen, and two pore-pressure ports were inserted into the sleeve (shrink sleeve). The axial deformation of the specimen was measured by two LVDTs, and from the chain extensometer wrapped around the specimen, the radial strain was obtained.

An 8-mm-outer-diameter aluminum tube, representing a casing, was inserted into the 10-mm-diameter hole of the specimen. The casing was heated by an electrical heating element (200 W) that was inserted into the casing. The casing was closed at the bottom for two reasons: (i) the hole and the casing were initially filled lamp oil and the oil in the annulus was subsequently replaced by flowing brine from the bottom to the top. With the closure at the bottom of the casing and the brine spill point below the top of the casing, the electrical heating element and the wires were not getting into contact with brine to avoid a shorting of the heating element; (ii) in order to measure the annulus permeability and to observe if a hydraulic barrier has formed, a pressure difference between the bottom and the top of the hole was applied, so it is important that there is no flow through the inside of the casing.

As shown in Fig. 3, before exposing the specimens to brine, a few MPa confining stress was applied to prevent swelling. Subsequently, both the confining pressure and the pore pressure were ramped up to the stress state the heating tests were carried out. The experiments were carried out under hydrostatic stress conditions, and the pressure in the hole was the same as the pore pressure on the external lateral surface of the specimen. Heating cycles were performed after the specimens were consolidated (stable LVDT and radial strain signals), and the pore pressure inside the specimen had equilibrated. The temperature of the heating elements was varied between 100 and 400 °C. Before and after the heating cycles the annulus permeability was measured by applying a small pressure differential (0.12 MPa) along the annulus (induced by sudden small dead-volume changes) and measuring the decay of the pressure differential due to annulus flow (during the permeability measurements the valves in the fluid lines that connect the upper and lower end of the borehole to a pump were closed to reduce the dead volumes at the upper and lower end of the borehole to well-defined values). The details of the measurement of the annulus permeability can be found in the work by Fjær et al. (2018).

Experiments were carried out both with Pierre shale (outcrop) and a field-shale from the North Sea. Mineralogical properties are measured in the lab and summarized in Table 2.

3 Experimental Results

3.1 Pierre-shale Test

In this test, the pore pressure and the borehole pressure were set to 6 MPa and kept constant throughout the test. The confining pressure was initially set to 14 MPa, then stepwise increased to 16 MPa and 17 MPa, after that it was decreased again to 14 MPa, with heating sequences at each confining pressure. The maximum confining pressure was still slightly below the confining pressure at which borehole failure was expected based on the results from previous hollow-cylinder tests with the same material. As pore fluid, brine with 3.5 wt% NaCl was used. It turned out that no hydraulic barrier was formed by borehole heating despite the evidence for thermally induced rock failure; the annulus permeability measurements did not indicate any measurable reduction in permeability throughout the test. The time-evolution of the test is shown in Fig. 3. It is evident that during the increase (decrease) of confining pressure the pore pressure inside the sample increases (decreases), followed by pressure equilibration due to drainage into the borehole and the outside of the sample that is held at constant pressure (6 MPa).

In Fig. 4, the measured temperature, pressure responses, and strain are shown as curves for the different heating sequences at different confining pressures and for different heating-element temperatures. The heating-element temperature, noticed in each subplot, is controlled by the apparatus rather than a measurement. Note that the temperature response at the casing behaves abnormal, as the recorded value here is smaller than that at the radius 16.25 mm.

By inspecting the pore-pressure response inside the sample for the different heating temperatures and confining pressures, it is noted that close to the borehole, the pore pressure strongly increases but reaches a maximum value that depends on the confining pressure: the maximum pore pressure increases with confining pressure. This indicates that the rock is reaching the failure envelope and deforms plastically. After the maximum pore pressure has been reached, the pore pressure starts to drop even though the temperature is still increasing. The pressure drop can be attributed to dilatancy during failure and the formation of fractures (brittle failure) resulting in enhanced drainage. Post-test CT images confirm the presence of brittle failure around the borehole (see Fig. 5). Prior to failure, thermal pressurization coefficient is approximately 0.12 MPa/ °C, which is consistent with thermo-poroelastic theory.

It is interesting to note that the pressure recordings at 38.75 mm always show a slight pore-pressure reduction

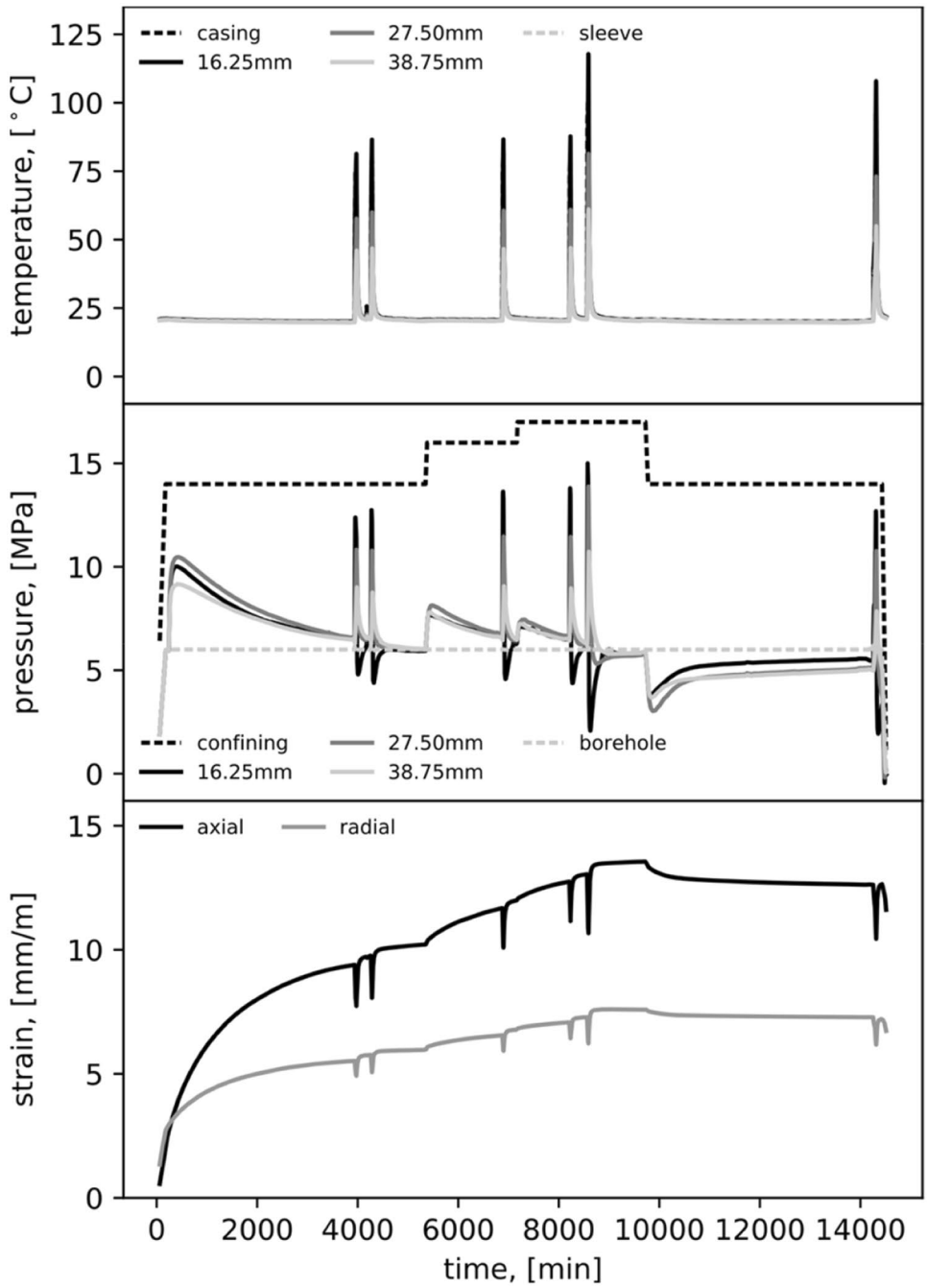

Fig. 3 Time-evolution of the Pierre shale test

Table 2 Mineralogical properties of the shales

Shale	Depth (m)	Total clay content (%)	Smectite content (%)	Quartz (%)	TOC (%)
Pierre-1	outcrop	47.9	5	26.6	1.1
Field-shale	1400	85.2	67	5.3	3.3

TOC total organic content

just at the moment when the borehole is being heated (see the solid lightest grey curve in Fig. 4). A similar phenomenon is also reproduced by the numerical simulations in Sect. 4. Such non-monotonous development of pore pressure is known as the Mandel-Cryer effect (Mandel 1953; Cryer 1963), which is a consequence of poroelastic coupling and the fact that a local deformation has an immediate consequence for stresses in the surrounding rock while a local pore pressure disturbance needs some time to propagate into the surroundings. Before the temperature starts to increase further away from the borehole, resulting

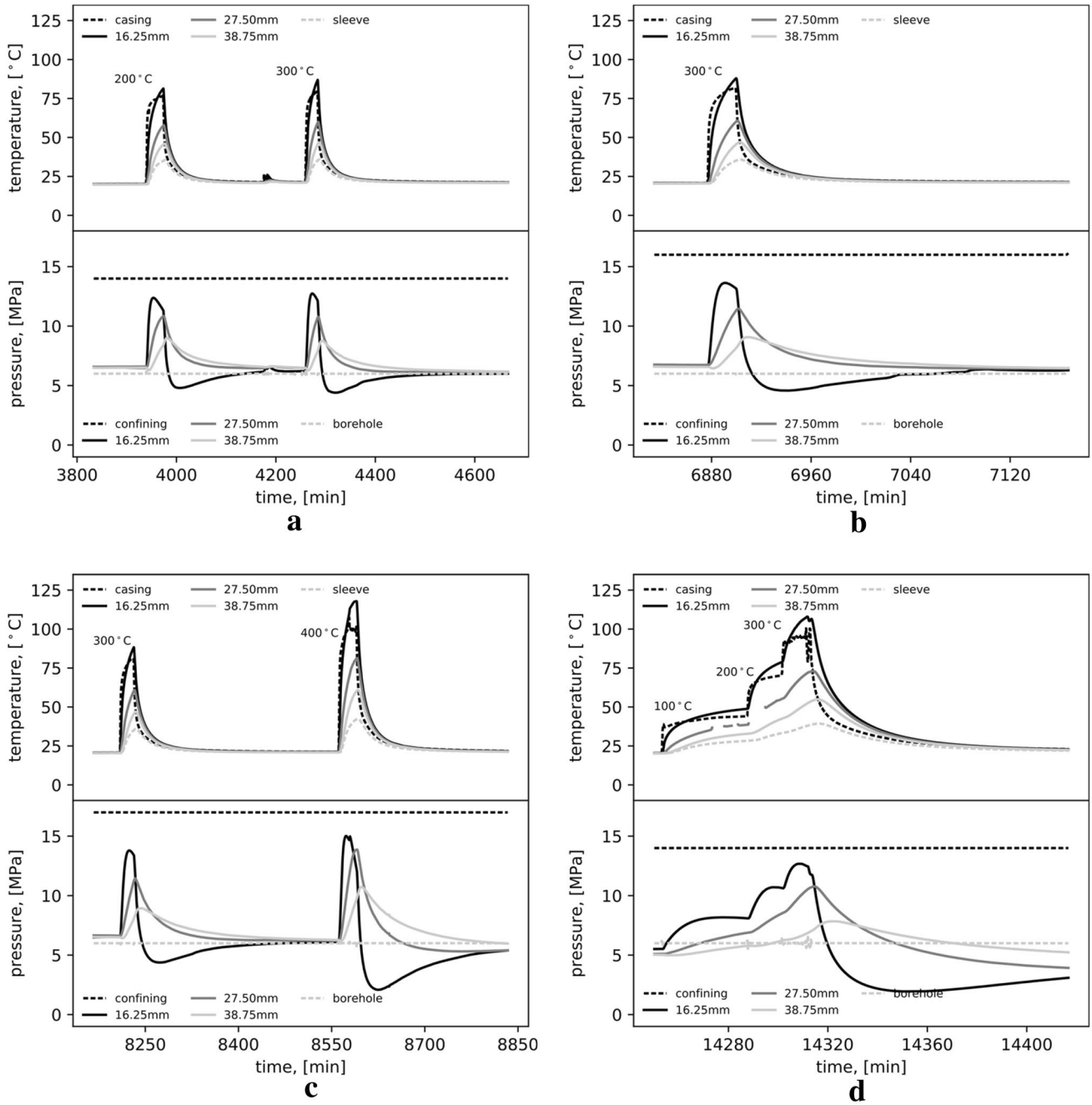

Fig. 4 Heating sequences at $p_{conf} = 14$ MPa (**a**), 16 MPa (**b**), 17 MPa (**c**), and reduced to 14 MPa (**d**) for the Pierre shale

in a pore-pressure increase, the heating-induced expansion of the area close to the borehole results in stress and strain changes outside the heated zone that results in a pore-pressure decrease: For an isotropic specimen with infinite diameter, it can be shown that the mean stress outside the heated zone is maintained. However, for a specimen with a finite diameter, with the confining pressure kept constant, the mean stress is reduced close to the outer surface of the specimen, which results in an increase in pore volume and thus a pressure reduction (under undrained conditions).

Note that during cooldown, the pore pressure at positions close to the borehole drops below the initial pore pressure, which is attributed to heating-induced dilatancy and/or enhanced drainage. During cooldown, a more elastic response is expected, which means that the rock dilation during rock failure is not reversed (or only partly), resulting in

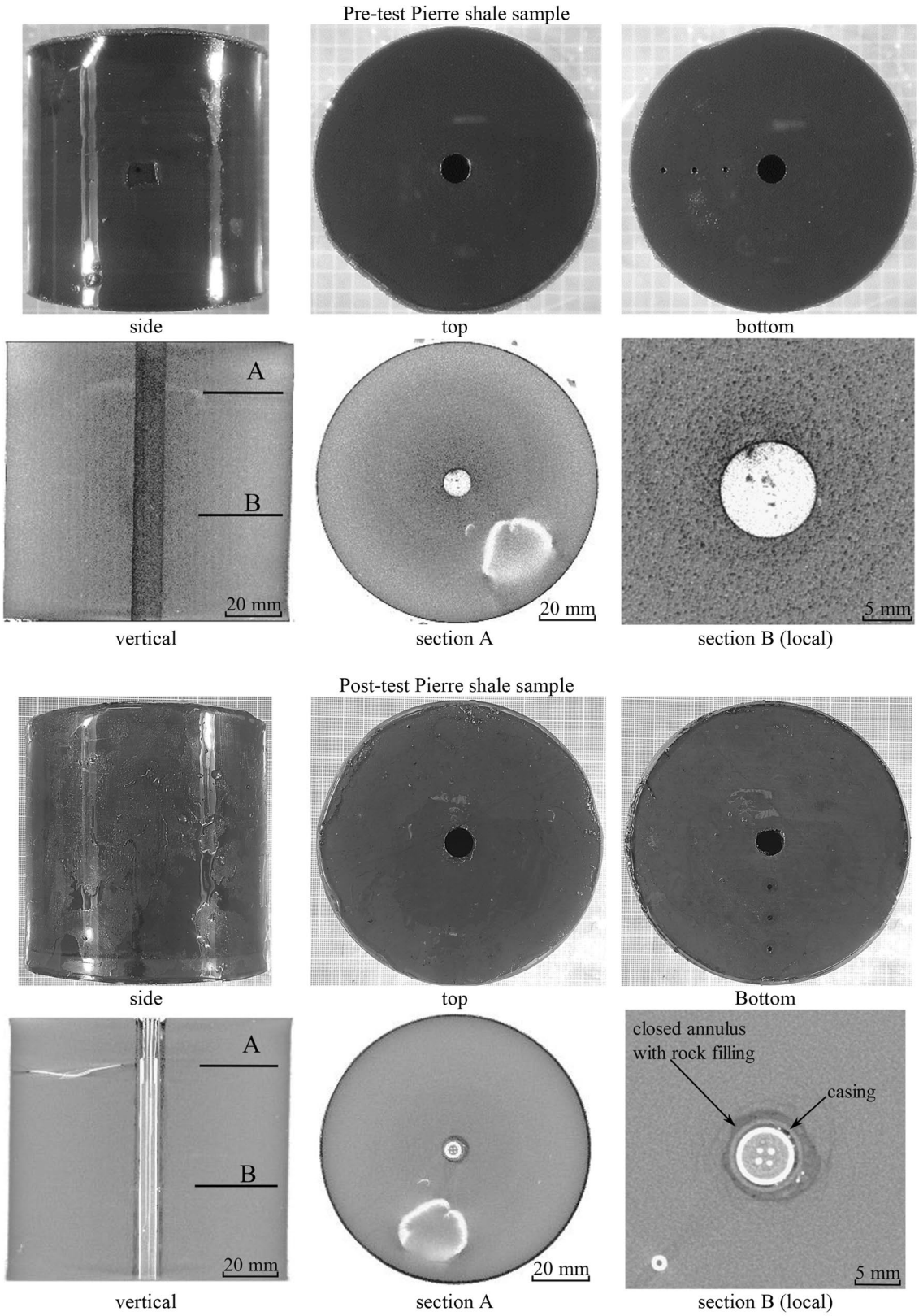

Fig. 5 Pre- and post-test photographs and CT images of the sample for Pierre shale

a pressure drop (in the present case by up to 10 MPa) that is larger than the pressure increases during heating. Actually, the observed pressure drop during cooldown is in accordance with the expected poroelastic response in the absence of plasticity effects. The observation of pore pressures below the initial pore pressure after a heating/cooling cycle is another strong indication for heating-induced rock failure.

Post-test CT images of the sample clearly show that heating has resulted in borehole failure and partial closure of the annulus (see Fig. 5). This also explains why there was some resistance when pulling out the casing after the test. However, it is obvious that no shale barrier was formed. The sample failed in a brittle way, and the average displacements on the borehole wall were not high enough to form a hydraulic barrier.

3.2 1st Field-shale Test

The 1st field-shale test was carried out at a confining pressure of $p_{\mathrm{conf}} = 25.8$ MPa and pore pressure and borehole pressure of $p_{\mathrm{f}} = p_{\mathrm{bh}} = 22.6$ MPa, which corresponds approximately to the in-situ stress conditions at the location the shale core was taken from. The temperature of the sample was brought to around 40 °C (in-situ temperature is about 46 °C). As pore fluid, brine with 3.4 wt% NaCl was used. The time-evolution of the test is shown in Fig. 6. As seen in the time-evolution, during the consolidation phase, the pore-pressure pump stopped working, which resulted in a decrease of pore pressure and borehole pressure (both are controlled by the same pump) by about 3 MPa before the initial pressure was re-established again. Based on experience from previous tests with material from the same shale core, it is unlikely that this pressure drop has caused borehole failure, but it cannot be fully excluded. An annulus permeability measurement confirmed full hydraulic communication through the annulus.

In Fig. 7, the measured temperature and pressure responses are shown during the stepwise heating sequence, where the temperature of the heating element was increased to 100 °C, 200 °C, 300 °C, and 400 °C (the heating element failed at the last stage). The temperature inside the sample at the measuring point closest to the borehole (11 mm from the borehole wall) increased by about 66 °C throughout the heating sequence, while at the measuring point furthest away from the borehole (33 mm from the borehole wall), the temperature increased by only 13 °C. The pore-pressure response was qualitatively the same as for Pierre shale. However, the pore-pressure increase close to the borehole was much smaller than for Pierre shale. This is less likely due to the different types of shale but rather due to the different stress states. For field-shale, the pore pressure is only 3.2 MPa smaller than the confining pressure (in the field, the shale is over-pressured), while in the Pierre-shale test it was 5–8 MPa. The pore-pressure data clearly shows that at the location of the innermost pressure sensor, the pressure does not exceed 24.2 MPa. Since the field-shale is more ductile compared to Pierre shale it can be assumed that the rock dilates, and the increase in pore volume balances the heat-induced fluid expansion, keeping the rock on the failure envelope. As for the field-shale, a thermo-poroelastic model that does not include plasticity effects can only account for the pore-pressure response during the 1st heating stage (heater element at 100 °C) where the thermal pressurization coefficient amounted to 0.11 MPa/ °C, similar to that found for Pierre shale. At higher heating temperatures, the pore-pressure response is strongly influenced by plastic rock deformation (see Sect. 4 for numerical simulations). It should be noted that the maximum increase in pore pressure at the position of the outermost pressure sensor is almost the same as at the position closest to the borehole even though the local temperature increase is by a factor 5 smaller. Note that the pore pressure prior to heating is not the same at the three internal pore-pressure sensors, which is probably an experimental artifact since there was sufficient time for pressure equilibration prior to borehole heating. Note that there is a temperature offset in the casing-temperature data. This offset is due to the wrong wiring of the corresponding thermocouple between two electric feed-throughs inside the cell.

With a thermal pressurization coefficient of 0.11 MPa/ °C, at the position of the innermost sensor, one might have expected a pore-pressure drop of about 6.6 MPa upon cooldown from 106 °C back to 40 °C since elastic rock deformation could be expected during cooldown, as observed for Pierre shale. However, the pore-pressure drops by only slightly more than 2 MPa. The pore pressure after the cooldown is lower than before heating, which indicates that non-reversible rock dilatancy has occurred during heating. However, either the rock dilation was partially reversible (opening and closing of cracks), or the permeability during cooldown was enhanced resulting in inflow from the borehole, possibly due to the presence of cracks formed during heating.

The fact that no barrier was formed upon heating indicates that the thermally induced plastic strain was not high enough. The in-situ shear stresses around the borehole are rather small for the given field-shale (due to the overpressure in the shale formation). The failure point is therefore close to the tensile failure criterion where dilatancy is expected to increase. Higher dilatancy and tensile fractures would result in enhanced pore-pressure decrease which counteracts the heating-induced pore-pressure increase, which may limit the total amount of plastic rock deformation. Another reason is that the particular field-shale is rather soft (Young's modulus is on the order of 0.1 GPa), which means that the thermal pressurization coefficient is small and only small thermal stresses are established that would increase the shear stress

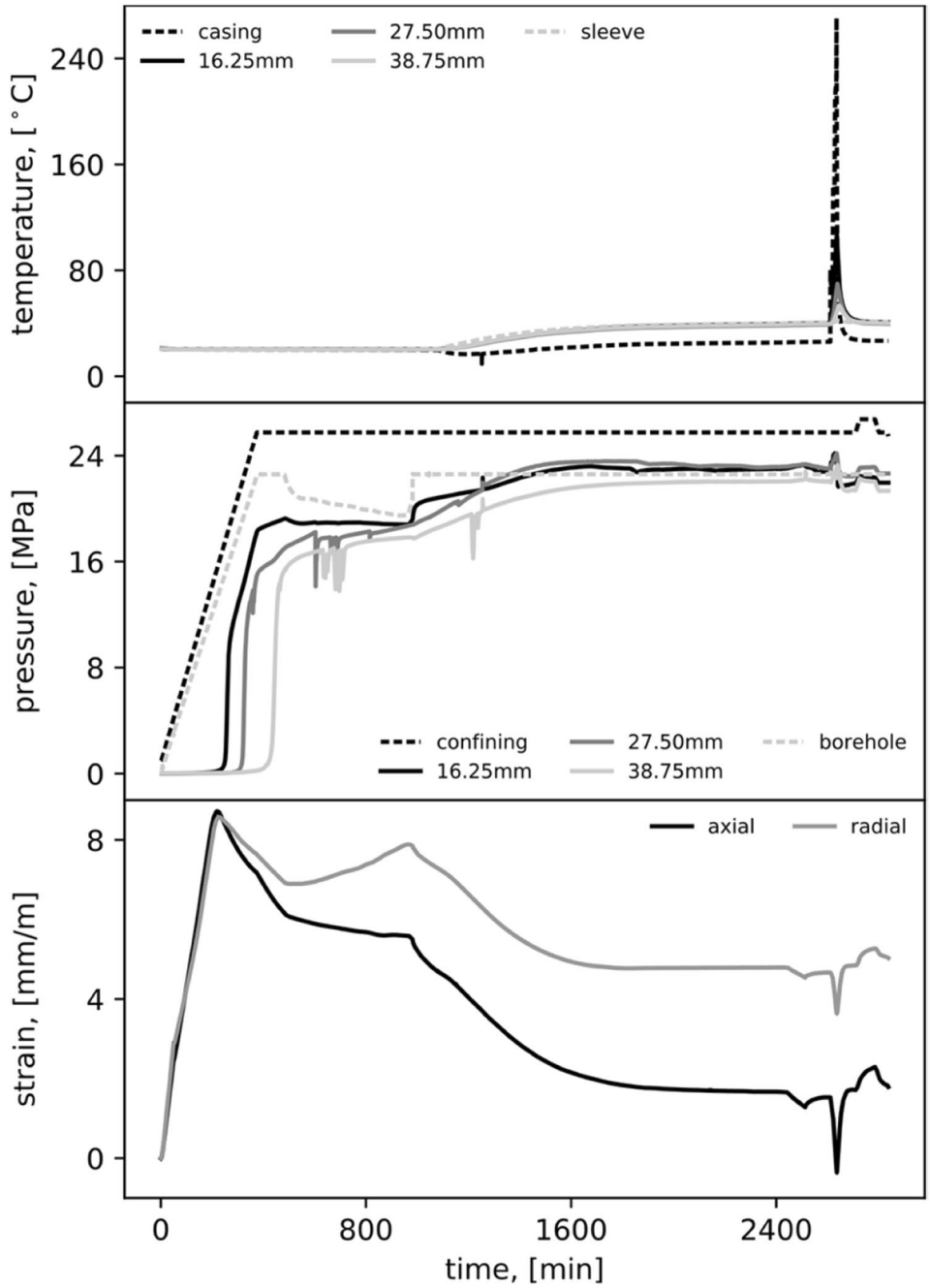

Fig. 6 Time-evolution of the 1st field-shale test

around the borehole and hence move the failure point further away from the tensile failure.

Pre- and post-test photographs and CT images of the sample are shown in Fig. 8. As revealed by the post-test CT images, the annulus around the casing is nearly closed. However, some open cracks are seen as an indication of brittle/tensile failure. The presence of cracks explains hydraulic communication along the annulus. We cannot exclude the possibility that the plastic deformations around the borehole happened during the initial loading of the sample, or during the borehole-pressure decline by about 3 MPa during the consolidation phase when the pore-pressure pump stopped working. However, in previous hollow-cylinder tests with the same shale type, borehole failure and casing contact was only observed when the borehole pressure was reduced by more than 7.5 MPa. It is therefore likely that the observed rock deformation around the casing was induced by heating.

3.3 2nd Field-shale Test

The results of the 1st field-shale test showed that borehole heating caused rock failure around the borehole and low

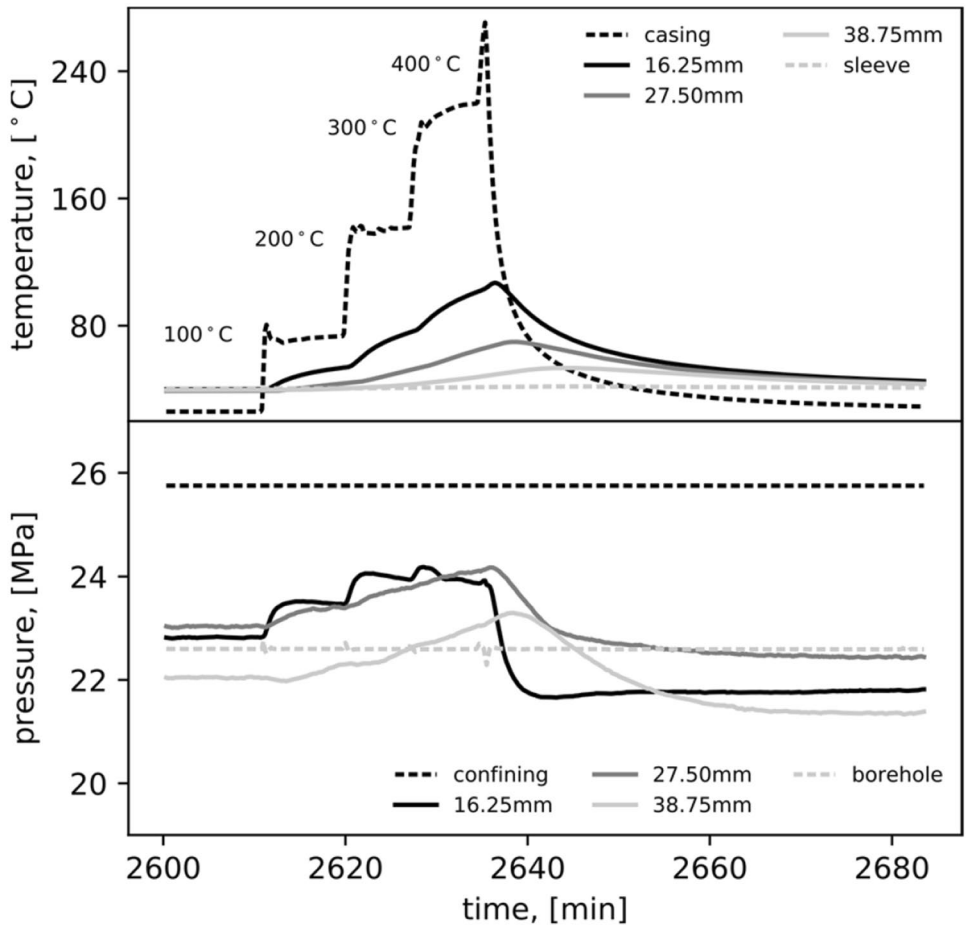

Fig. 7 Stepwise heating sequence of the 1st field-shale test

plastic deformations, which was attributed to both a small rock stiffness resulting in small thermal stresses and small effective stresses. Here, the effective stress denotes the difference between confining pressure and initial pore pressure. Small effective stress results in small shear stress and rock failure close to the tensile failure.

In order to check the hypothesis that higher effective stresses would result in enhanced heating-induced rock deformations and shale-barrier formation, a 2nd test was carried out with the same field-shale at higher effective stress: The same confining pressure was applied (p_{conf} = 25.8 MPa), and pore pressure and borehole pressure were reduced by 1.3 MPa to $p_f = p_{bh}$ = 21.3 MPa. As pore fluid, brine with 3.5 wt% NaCl was used. Other than for the 1st field-shale test, the compaction cell was kept at room temperature; in this way, a larger change in temperature during heating could be realized since previous tests showed that the heating elements often failed at temperatures above 300 °C. To what extent the initial temperature of the rock could affect the results of borehole heating is to be investigated in a separate study.

The time-evolution of the test is shown in Fig. 9, and the two subsequent heating cycles were carried out (Fig. 10). In the first heating cycle, the temperature of the heating element was increased in steps to 100 °C, 200 °C, and 300 °C. After several minutes at 300 °C the heating element was switched off and the sample cooled down. In the second heating cycle, the temperature of the heating element was increased in one step to 300 °C. Note that the signal of the temperature sensor closest to the borehole was unstable at high temperatures.

The pore-pressure response to heating inside the sample is qualitatively similar to the response measured in the 1st field-shale test: Close to the borehole the pore pressure increases rapidly (with a thermal pressurization coefficient of 0.1 MPa/ °C, similar to that of the first test) until a certain maximum pressure is reached. Subsequently, the pore pressure gradually decreases while the temperature is still rising, which is attributed to rock failure and dilatancy. In the present test, however, the annulus pressure and initial pore pressure were lower than in the 1st field-shale test, and the maximum increase in pore pressure was larger. On the other hand, rock failure occurred at a lower pore pressure: while in the 1st field-shale test the pore pressure exceeded 24 MPa, in the present test during the first heating cycle, it only reached a maximum value of 23.3 MPa at a distance

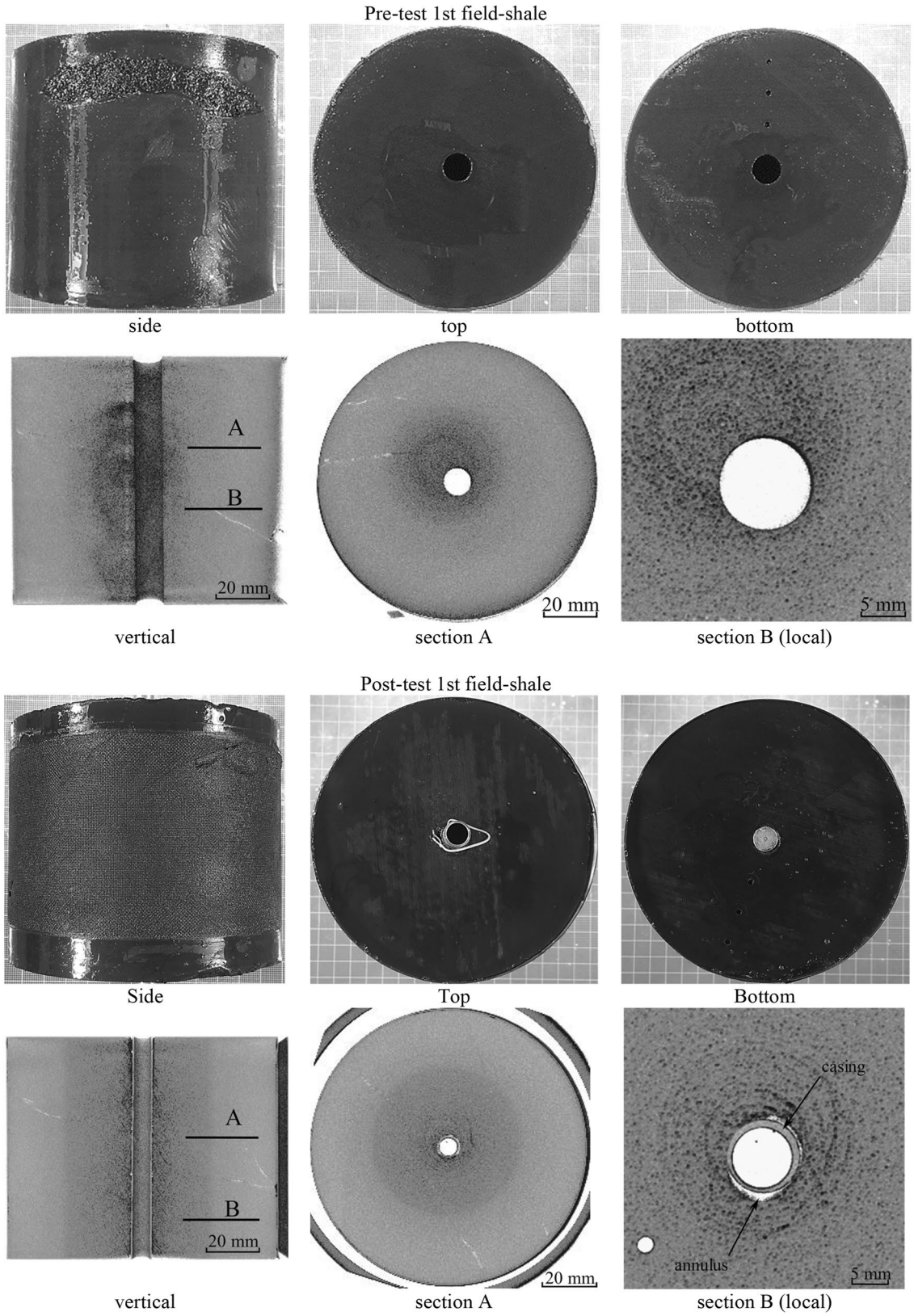

Fig. 8 Pre- and post-test photographs and CT images of the sample for the 1st field-shale test

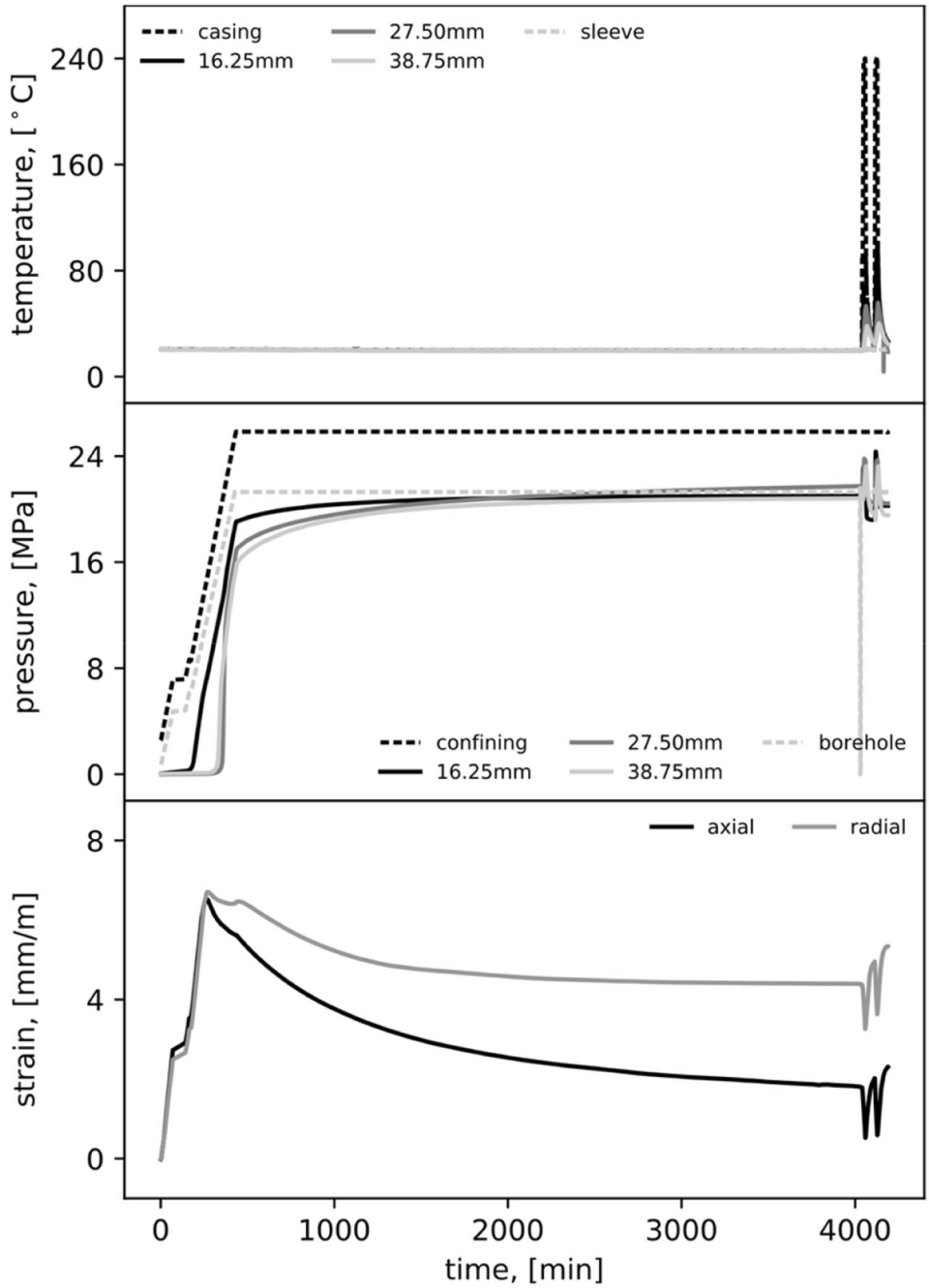

Fig. 9 Time-evolution of the 2nd field-shale test

from the borehole axis of 16.25 mm (closest sensor to the borehole) and 23.8 MPa at a radius of 27.5 mm. This agrees with our expectations as shear stresses around the borehole are higher in the present test as compared to the 1st field-shale test (same confining pressure, lower annulus pressure, resulting in a larger Mohr circle), which means that rock failure occurs at a smaller absolute pore pressure. The total amount of plastic deformation depends on the temperature change and the duration of heating, but it also depends on the degree of dilatancy, which decreases with increasing shear stress and larger distance from the tensile strength of the failure envelope. This may explain the enhanced plastic deformation and annulus closure in the present test. In fact, the first heating cycle resulted in a measurable reduction of the annulus permeability from 10 mD to about 2 mD (see Fig. 11) whereas no measurable reduction of annulus permeability was observed in the 1st field-shale test.

During the second heating cycle, the pore pressure at the innermost sensor reached 24.3 MPa, about 1 MPa more than during the first cycle, while further away from the borehole, the maximum pore pressures were similar to those reached during the first heating cycle. This increase in pore pressure

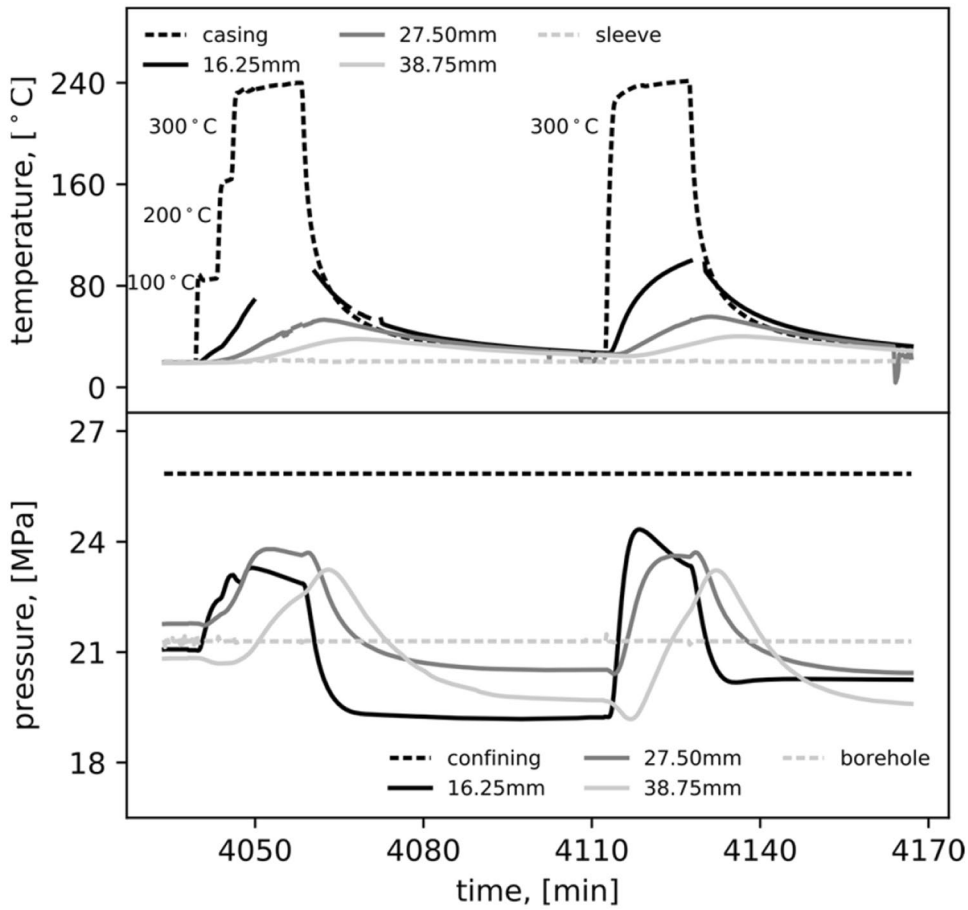

Fig. 10 Stepwise heating sequences of the 2nd field-shale test

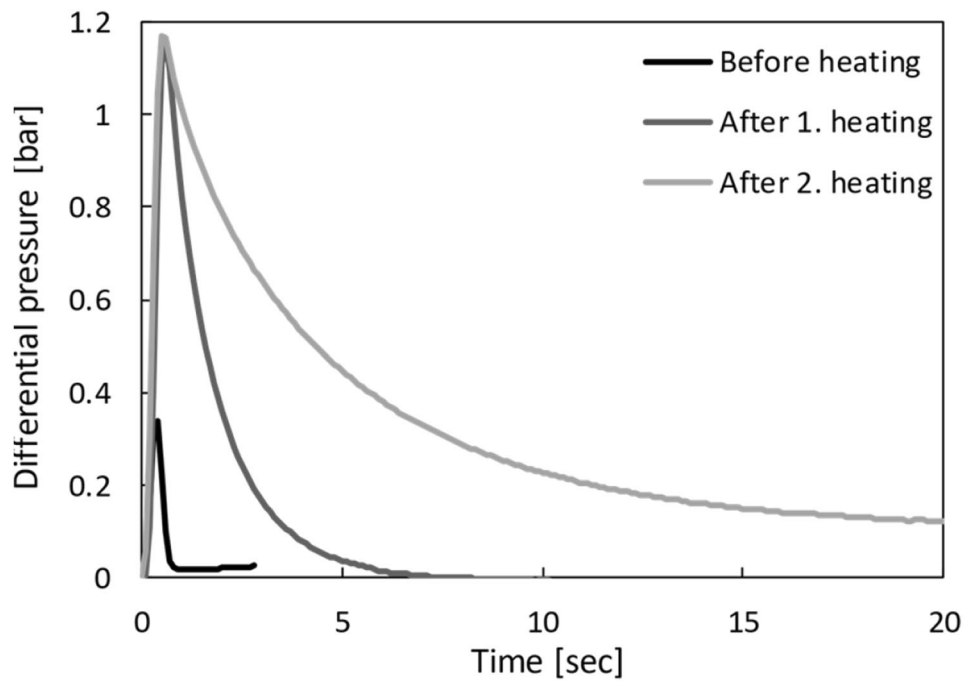

Fig. 11 Results of pressure pulse-decay measurements of the 2nd field-shale test before/after each heating cycle from which the annulus permeability can be estimated

close to the borehole can possibly be explained by the closure of the annulus during the first heating cycle and the build-up of radial stress during the second heating cycle, resulting in reduced shear stress and hence higher pore pressures to bring the rock to failure. It turned out that the second heating cycle resulted in a further reduction of the annulus permeability to approximately 0.2 mD (see pulse-decay data in Fig. 11). The obtained annulus permeability is still about an order of magnitude higher than the permeability of cement and would therefore not be low enough for a shale barrier. However, the present test shows that heating under the right conditions can result in annulus closure and significantly reduce the annulus permeability. Further studies are needed to find out how the annulus permeability can be further reduced (multiple heating cycles, higher temperatures, etc.) to form a shale barrier with a permeability on the order of 0.01 mD.

Overall, the temperature and pore-pressure data from the 1st and 2nd field-shale tests seem to be consistent within a certain variability of rock properties, and the differences in pore-pressure changes and plastic deformations around the borehole can be attributed to the different stress, pore-pressure, and annulus-pressure conditions under which the tests were performed.

The pre- and post-test photographs and CT images are shown in Fig. 12. While in the upper and lower part of the sample the annulus is still open, it is closed in the center part of the sample where the heating is strongest (at the top and the bottom the sample is in contact with the steel endcaps that act as heat sinks). But even in the central part of the sample, there are some small openings and cracks visible in the CT images that explain why a full hydraulic seal was not achieved (it should be noted that the images were taken after the confining pressure was relieved and the sample was dismounted so that some of the cracks could have formed during stress relief).

4 Numerical Simulations

The finite-element code ABAQUS is applied in this study aiming to best match the step-heating sequences of the lab tests described in Sect. 3, specifically to match the time-evolution of the temperature and the pore-pressure at the thermocouples and the pore-pressure sensors inside the samples. The following assumptions/simplifications are introduced: The rock is the only material simulated which is governed by the thermo-poro-elasticity with Mohr–Coulomb criterion (shear yield function) and a tensile failure function (see Chapter 1). Other components in the test, for example, the heating tool, endcaps, and the confining fluid are as accounted for by the corresponding boundary conditions. Isotropic in-situ stress and pore pressure are applied, and the rock is assumed to be isotropic and homogeneous, so the hollow cylindrical geometry can be simplified to an axisymmetric rectangle, which boosts simulation speed dramatically. Most of the material properties are assumed to be constant, except for the cohesion (plastic strain dependency), the thermal expansion coefficient of water (temperature dependency), and the water bulk modulus (temperature dependency). The material properties used in the simulations originate from two sources. Some properties are measured in the lab. For those properties that could not be measured locally, values of properties are referred from literature and public databases. Due to the rock heterogeneity, the parameters measured from the triaxial tests maybe not fully represent the samples tested in the current study. For the field-shale, the values of two properties (Young's modulus and permeability) are modified due to some uncertainty to quantify them, so that the current matches are achieved. Quantitative parameter fitting (such as the least-squares method) was not considered to be suitable for matching the lab-scale simulation and the lab results in this case. Instead, we applied the rule of thumb that the properties with confident sources were kept fixed and applied a 'trial and error' fitting procedure for those parameters with large uncertainty, aiming for a qualitative match. The purpose of this procedure was not to search for fine-tuned parameter values but to demonstrate that the applied model equipped with reasonable parameter values was able to reproduce the observations with reasonable precision. The set of parameters from the lab-scale simulation is then implemented in simulations with field-scale geometry to evaluate the potential of borehole closure in the field condition.

4.1 Simulations on the Basis of Lab Tests

The lab-scale simulations focus on the stepwise heating sequences (see Figs. 4d, 7, 10). In the simulations, the hollow cylindrical specimen is simplified as a rectangle by assuming axisymmetric geometry (see Fig. 13). The element size is 1 mm by 1 mm. 50 elements are distributed evenly along the radial direction, and 100 elements are distributed evenly along the axial direction. Initially, the pore pressure and temperature are constant everywhere inside the specimen. The hydraulic confining pressure, the borehole pressure (equivalent to the pore pressure at the borehole), and the pore pressure are kept constant on the boundaries during heating. From the borehole axis to the outer boundary, the positions of the sensor are named S1, S2, and S3 for convenience.

The initial conditions, the boundary conditions, the constitutive parameters, and the stepwise heating sequence are summarized in Tables 3, 4, 5, 6, 7, 8. The initial conditions, the boundary conditions, and the stepwise heating sequence correspond to the lab tests in the previous section.

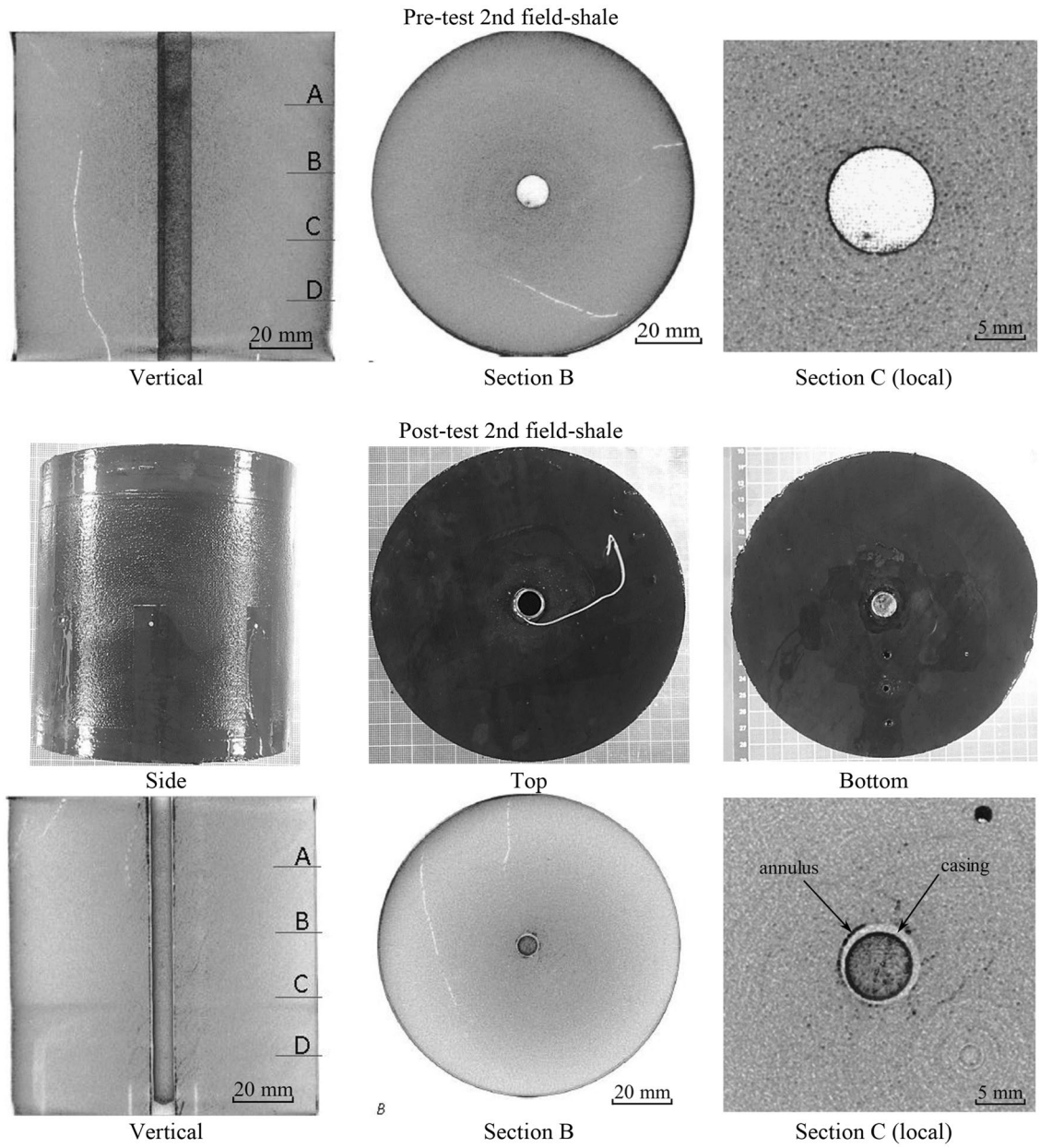

Fig. 12 Pre- and post-test photographs and CT images of the sample for the 2nd field-shale

The constitutive parameters (rock density, porosity, Young's modulus, Poisson's ratio, grain bulk modulus, internal friction angle, and dilation angle) were measured in the lab with material from the same rock. Cohesion hardening/softening is modified, based on results from triaxial lab tests, to match the pore pressure data in this study. Permeability is also evaluated based on the tests in this study. Tensile strength is assumed very low for soft rocks such as shale. Sharqawy et al. (2010) and Nayar et al. (2016) investigated the correlations of seawater properties with respect to salinity, temperature, and pressure based on a series of lab tests, from which we determined the pore fluid properties (density, specific heat capacity, conductivity, dynamic viscosity, and thermal expansion coefficient). Robertson (1988) provided rock-related specific heat capacity, conductivity, and thermal expansion coefficient. The water bulk modulus was evaluated based on the work by Batzle and Wang (1992).

4.1.1 Simulation of Pierre-shale

Figure 14 shows the match of temperature time-evolution based on the stepwise heating sequence of Pierre shale. The temperature match at S1 (the innermost sensor) is fairly good. At S2 (the intermediate sensor) and S3 (the outermost

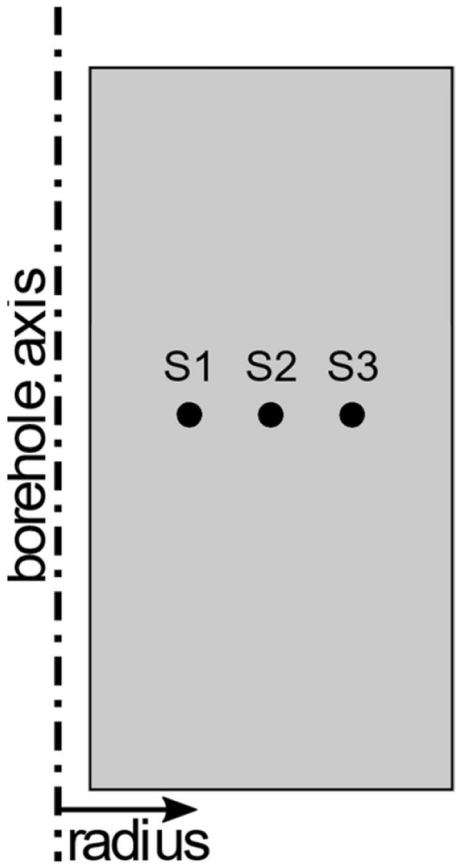

Fig. 13 The axisymmetric geometry of the hollow cylindrical sample. Three dots indicate the positions of sensors located at 16.25 mm (S1), 27.50 mm (S2), and 38.75 mm (S3) from the borehole axis

Table 3 Initial condition and boundary condition

Initial/boundary condition	Pierre shale	1st field-shale	2nd field-shale
Initial temperature (°C)	20.0	40.0	19.6
Initial pore pressure (MPa)	6.0	22.6	21.3
Borehole pressure (MPa)	6.0	22.6	21.3
Confining pressure (MPa)	14.0	25.8	25.8

sensor), the temperatures are slightly underestimated. Matching the pore pressure response is difficult since the rock failure has a strong impact on the pore pressure. Nevertheless, given all the uncertainties of the plasticity model and the experimental errors, we believe that Fig. 15 shows the acceptable pore pressure match. Figure 16 shows the thermally induced enlargement of the plastic zone at the end of each heating step and subsequent holding sequence. These three moments are denoted as A, B, and C in Fig. 14. At the end of the simulation, S1 is located inside the plastic zone.

4.1.2 Simulation of the First Field-shale

Figures 17, 18 show the temperature and the pore pressure match for the 1st field-shale. The temperature match is even better than that of the Pierre-shale, but the pore pressure was more difficult to match. Especially during the last holding sequence at S1, the measured pore pressure decreases while the simulation shows an increase. By comparing the simulations of the 1st and the 2nd field-shale (shown in the next subsection), we conclude that the uncertainties of Young's modulus and the permeability, as well as the variation of permeability during heating ignored in the present simulations, play important roles in the simulation of the pore pressure.

4.1.3 Simulation of the Second field-shale

For the 2nd field-shale simulation, the stiffness (Young's modulus) had to be increased, and the permeability had to be decreased to get a good match with the experimental data (see Table 4). Figure 19 shows the match of temperature is still good enough, except part of the experimental data is not available at S1. In Fig. 20, the measured pore pressure at S1 is compared to the simulated ones with two permeabilities: 90 nD (dash) and 120 nD (dash-dot). At S2 and S3, only the pore pressure time-evolution simulated with 90 nD is shown (dashed line). The time-evolution of pore pressure with 120 nD is omitted in Fig. 20, as they behave similarly to those of 90 nD with a lower increase of pore pressure and a quicker diffusion. As for the first sample, matching of the pore pressure response at S1, S2, and S3 was a challenge. For this sample, we tried to obtain a good match at S1 with the expense of large mismatches at S2 and S3.

The lab-scale simulations of the stepwise heating sequences reflect thermo-hydro-mechanical behavior of the saturated rock with elastoplastic failure: the first step of heating mainly induces thermal pressurization in the poroelastic medium and produces an elastic response; the second step of heating enhances the thermally affected zone around the borehole, and triggers thermally induced rock failure; the third step of heating intensifies the effect of thermal pressurization, resulting in more extensive rock failure and having a large impact on pressure diffusion.

4.2 Field-scale Simulation

The simulations in Sect. 4.1 aims to evaluate the constitutive parameters of the rocks to be applied in the field-scale simulations. The field-scale geometry is described in Fig. 21 as an axisymmetric rectangle with 31.1 cm

Table 4 Constitutive parameters

	Pierre shale	1st field-shale	2nd field-shale
Density—rock (solid grain) (kg/m^3)	2375	2691	2691
Density—fluid (kg/m^3)	1000	1000	1000
Specific heat capacity—rock (solid grain) [J/(kg K)]	900.0	940	940
Specific heat capacity—fluid [J/(kg K)]	4180	4021	4021
Conductivity—rock (solid grain) [W/(m K)]	1.13	0.76	0.76
Conductivity—fluid [W/(m K)]	0.60	0.66	0.66
Dynamic viscosity [10^{-3} kg/m/s]	1.00	0.35	0.35
Young's modulus (drained) (GPa)	1.00	0.13	0.53
Poisson's ratio (drained) (-)	0.30	0.42	0.42
Linear coefficient of thermal expansion—rock (10^{-5}/°C)	1.0	1.0	1.0
Linear coefficient of thermal expansion —water (10^{-5}/°C)	Table 5		
Porosity (%)	20.0	39.7	39.7
Grain bulk modulus (GPa)	36.20	16.07	16.07
Water bulk modulus (GPa)	Table 6		
Permeability, nano-Darcy	30	300	90 and 120
Internal friction angle (°)	30.00	12.00	12.00
Dilation angle (°)	13.00	8.47	8.47
Cohesion (MPa)	Table 7		
Tensile strength (MPa)	–	0.1	0.1

Table 5 Linear coefficient of thermal expansion—water

Temperature (°C)	Pierre shale (10^{-5}/°C)	1st and 2nd field-shale (10^{-5}/°C)
10	2.9	5.7
20	6.9	8.4
30	10.1	11.0
40	12.8	13.2
50	15.2	15.3
60	17.4	17.2
70	19.4	18.9
80	21.3	20.5
90	23.2	22.0
100	–	23.4
110	–	24.8
120	–	26.2

Table 6 Water bulk modulus

Temperature (°C)	Pierre shale, 1st, and 2nd field-shale (GPa)
0.0	2.06
20.0	2.27
48.9	2.35
93.3	2.19

Table 7 Cohesion hardening/softening versus equivalent plastic strain

Equivalent plastic strain (–)	Pierre shale (MPa)	Equivalent plastic strain (–)	1st, and 2nd field-shale (MPa)
0.000	1.4	0.000	1.20
0.001	1.5	0.101	0.68
0.002	1.6	0.380	0.68
–	–	0.480	0.48

(12–1/4 inch) borehole diameter, 3 m outer boundary, and 30 m height along the borehole axis. 21 elements follow a geometric sequence along the radial direction, and 1000 elements are distributed evenly along the axial direction. Instead of heating the entire borehole wall as in the lab-scale simulations, only a 10 m section in the center is heated in the field-scale simulations. All the field-shale inputs listed in Table 3, 4, 5, 6, 7 are used for the field-scale simulation, except for those as follows. The in-situ temperature applied here is 46 °C, and the in-situ vertical stress is 28.3 MPa based on the field assessment. Note that the in-situ horizontal stress equals to the confining pressure mentioned in Table 3. The heating process is fairly simple: The temperature at the borehole wall is increased linearly from in-situ temperature to the target temperature over 10 h, then the temperature on the borehole wall is held constant for the next 100 h. 250 °C is the target temperature in the benchmark simulation, which is changed in the range of 200–350 °C in the parametric analysis later.

Table 8 Heating-holding sequence

Stage	Pierre shale		1st field-shale		2nd field-shale	
	Stage time (min)	Temp (°C)	Stage time (min)	Temp (°C)	Stage time (min)	Temp (°C)
Initial	0.00	20.0	0.00	41.5	0.00	20.0
Heating 1	0.63	72.0	1.50	87.0	0.50	85.6
Holding 1	34.57	72.0	7.50	87.0	3.33	85.6
Heating 2	0.63	140.0	1.17	155.0	0.67	162.5
Holding 2	14.00	140.0	6.17	155.0	1.83	162.5
Heating 3	0.63	201.0	1.50	220.0	0.83	232.0
Holding 3	10.42	201.0	5.83	234.0	11.67	240.0

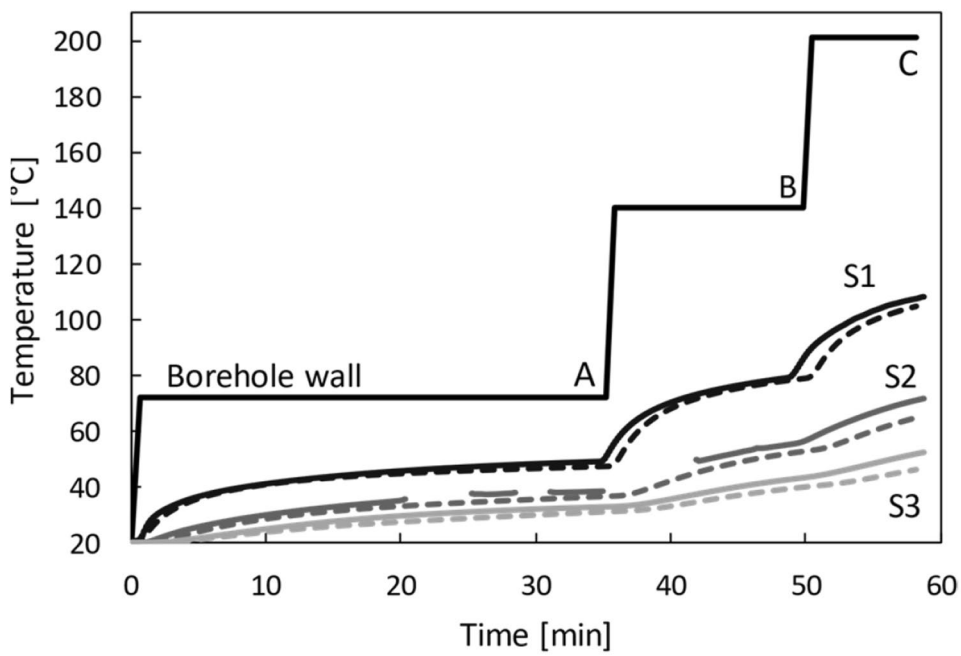

Fig. 14 Matching temperature time-evolution at S1–S3 for Pierre shale. Solid—experiment; dash—simulation

Figure 22 shows the thermally induced progressive borehole closure with field-scale geometry based on the rock properties obtained from the 1st and the 2nd field-shale laboratory tests (permeability for the 2nd field-shale is 90 nD). The results indicate that the properties of the 2nd field-shale sample (higher stiffness, lower permeability) lead to a larger reduction of the borehole radius and thus a higher potential for the formation of a shale barrier.

For a 9–5/8 inch (24.5 cm) casing in a 12–1/4 inch (31.1 cm) borehole, the width of the casing annulus is about 3.3 cm (20% of the borehole radius). Therefore, the simulated displacement at the borehole wall has to be larger than this value for a rock-casing contact (note that a casing is not included in the simulations, so the displacement at the borehole wall can exceed 3.3 cm). Figure 23 shows the thermally induced radial displacement at the borehole wall when the target temperature is held for 100 h, which indicates that for temperatures higher than 200 °C the rock around the casing is expected to get into contact with the casing.

5 Discussion

Based on the lab results and numerical simulations, several issues will be discussed first, which help to understand the thermally induced rock behavior. The simulation of thermal-induced pore pressure in elastic rock is helpful to address the importance of rock failure on pore pressure development. Several parametric analyses are shown after that. Note that the major purpose is not to reveal the most sensitive and dominant properties for reproducing lab results or field-scale borehole closure. Otherwise, parameters like the thermal expansion coefficient should have been considered in the parametric analysis. The parametric analyses of friction

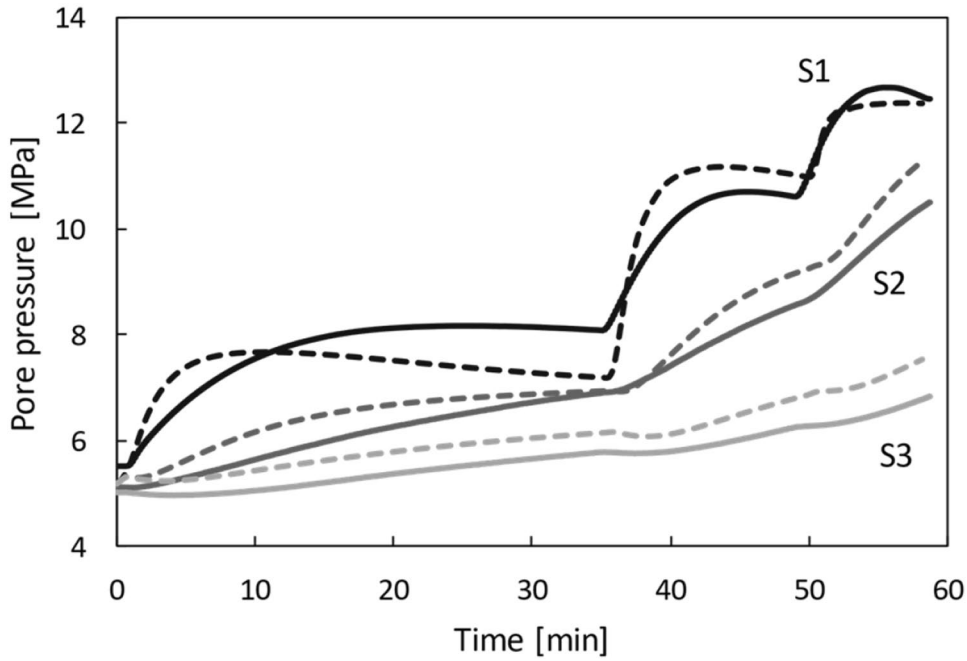

Fig. 15 Matching pore pressure time-evolution at S1–S3 for Pierre shale. Solid—experiment; dash—simulation

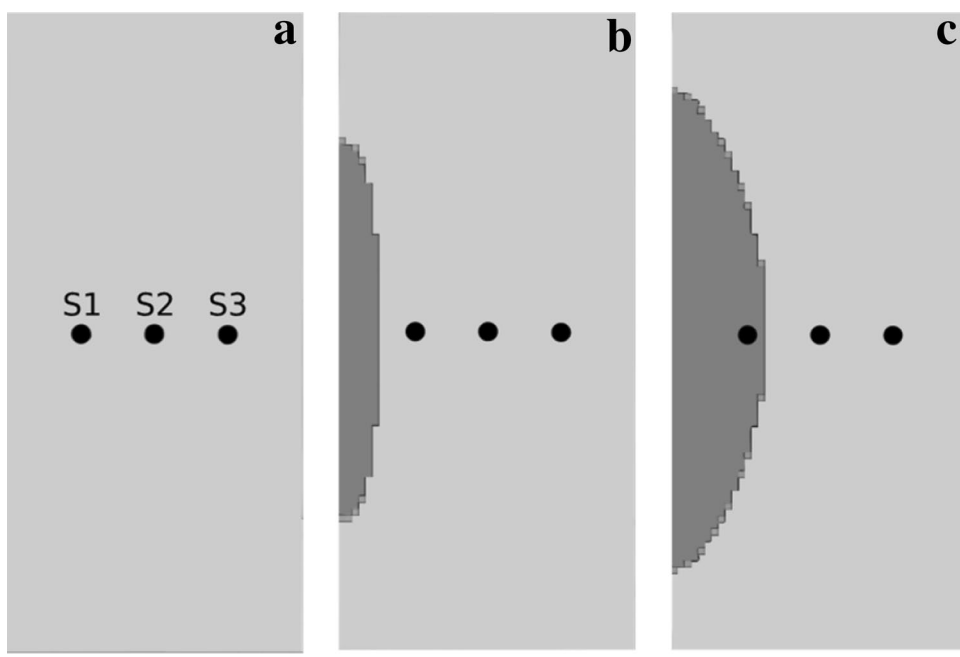

Fig. 16 Active plastic zone (dark grey) at the end of the holding sequences after each heating step for Pierre shale. Frames **a**, **b**, and **c** correspond to the moments shown in Fig. 14

angle and dilation aim to reveal whether shear failure or tensile failure happens or dominates the thermally induced rock yield. Young's modulus and permeability of the field shale are quantified with large uncertainty. The parametric analyses aim to show how large the uncertainty affects borehole closure. In the second part of this section, potential applications and future work are mentioned, regarding the heating source, rock-casing contact, shale creep, brittle/ductile failure, and borehole closure induced by decreasing annulus pressure.

The experimental interpretation in Sect. 3 indicates that heating can make the specimen fail around the borehole. Rock failure induces dilation and fracturing and enhances drainage, which prevents further increment of thermally induced pore pressure. If the heated rock did not fail, a higher pore pressure should have been observed. Figure 24 shows the pore pressure time-evolution considering purely elastic rock, in comparison to the observations and simulations shown in Fig. 18. At the innermost sensor in the first heating-holding stage, the pore pressure increment simulated

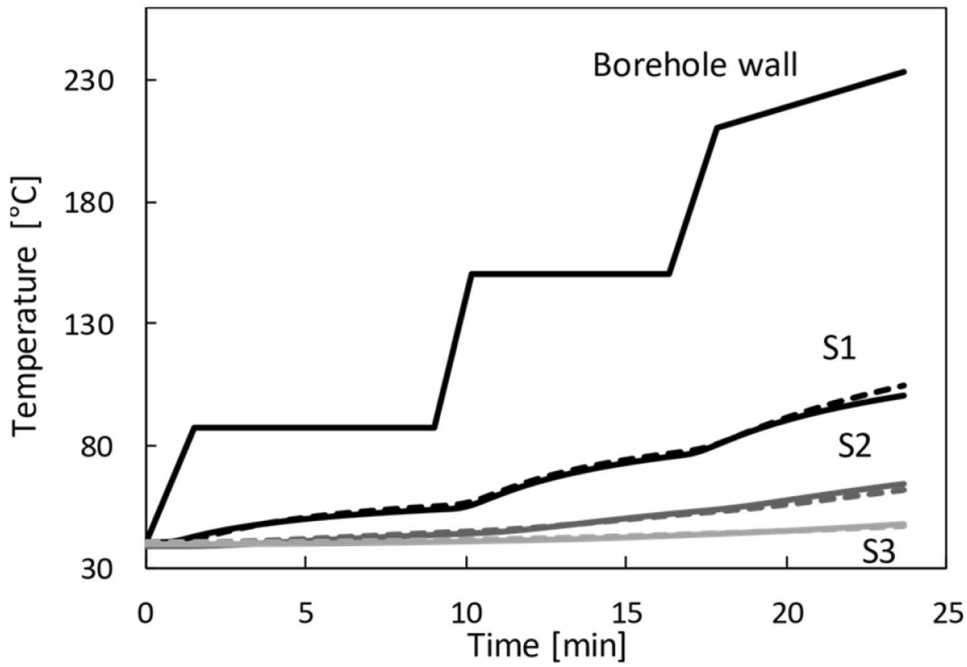

Fig. 17 Matching temperature time-evolution at S1–S3 for the 1st field-shale. Solid-experiment; dash-simulation

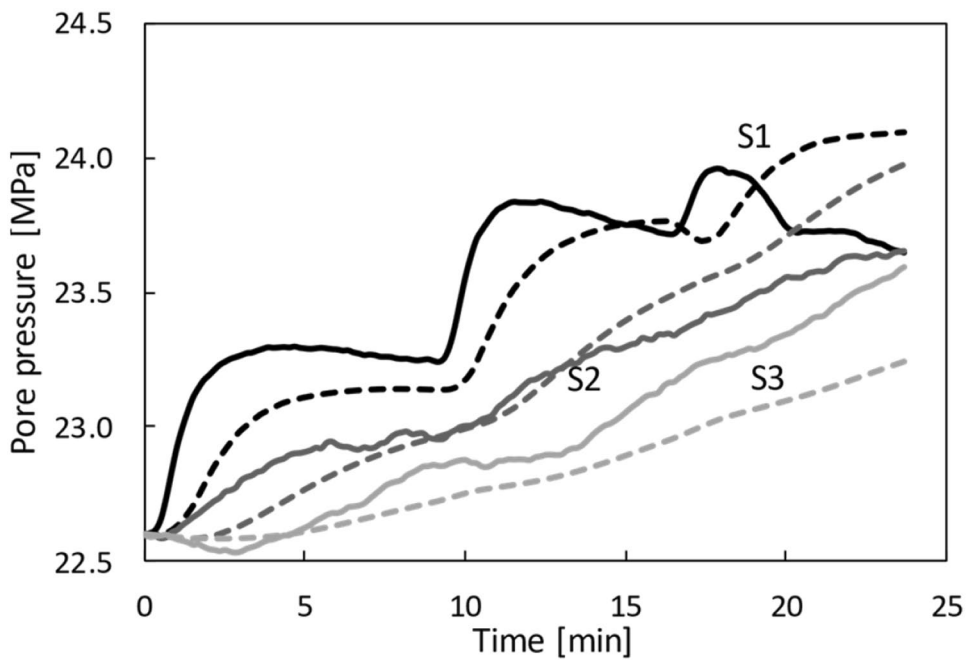

Fig. 18 Matching pore-pressure time-evolution at S1–S3 for the 1st field-shale. Solid-experiment; dash-simulation

in the elastic rock is consistent with the lab result, and the simulation result in elastoplastic rock. The temperature at this stage is not high enough so that the rock behaves elastically. As the heating temperature increases further in the second and the third stage, the simulated pore pressure in the elastic rock deviates from that of the lab result and the simulation in the elastoplastic rock. At the intermediate sensor, the two curves of simulations match each other well until the second holding stage. After that, the pore pressure in the elastic rock goes higher than that in the elastoplastic rock. This can be explained as an influence from the pore pressure at the innermost sensor. At the outermost sensor, the two simulation curves match each other well, since both behave elastically and the location is far from the innermost sensor. Figure 24 separates the poroelastic behavior from the poro-elastoplastic behavior, which indicates that the heating-induced rock failure is an important variable for the interpretation of the observations in the lab.

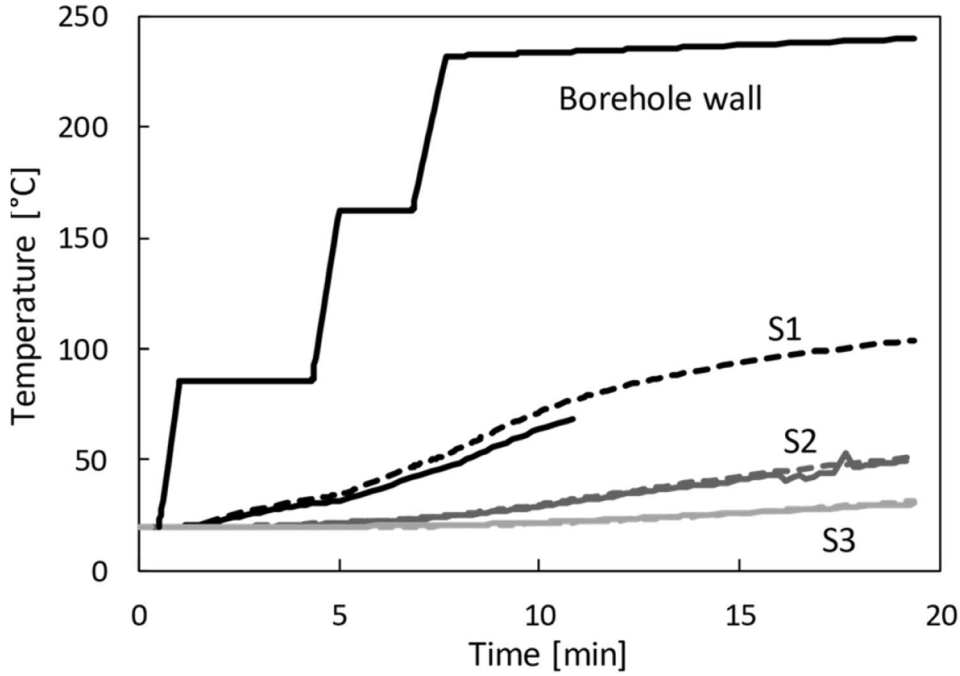

Fig. 19 Matching temperature time-evolution at S1–S3 for the 2nd field-shale. Solid-experiment; dash-simulation

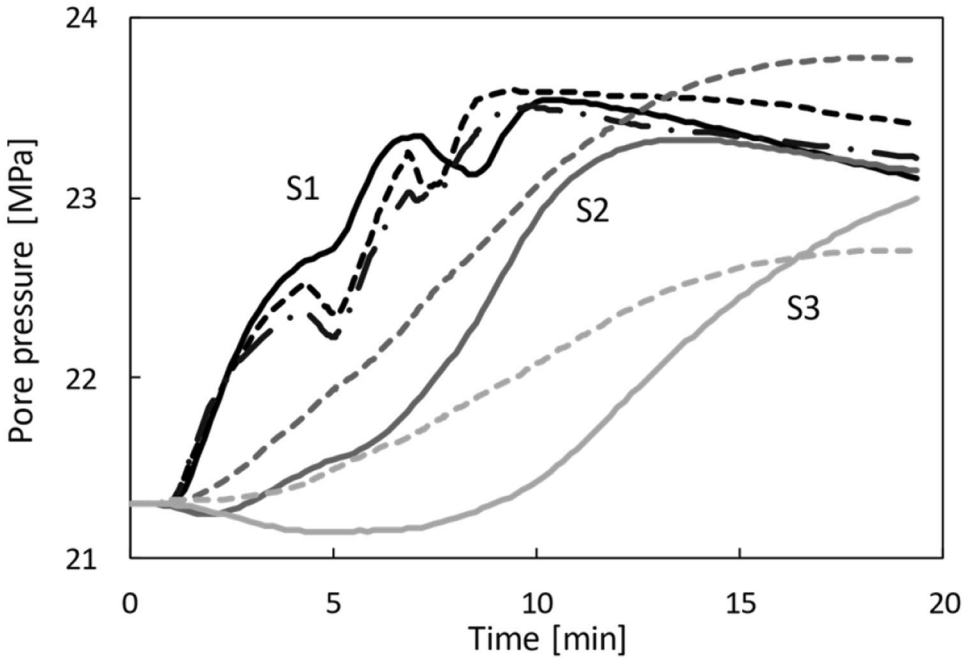

Fig. 20 Matching pore-pressure time-evolution at S1–S3 for the 2nd field-shale. Solid-experiment; dash-simulation with 90 nD; dash-dot: simulation with 120 nD

The experimental analysis of the 1st field-shale (see details in Sect. 3.2) indicates that the effective stress of rock failure around the borehole is near the tensile failure, which further implies that the borehole closure should be insensitive to the internal friction angle, the critical parameter of the Mohr–Coulomb criterion. Graphically, referring to the situation of a small Mohr circle in Fig. 1, the thermal pressurization decreases the effective stress but keeps the shear stress nearly the same, which results in the Mohr circle shifting to the left, and tensile failure or shear failure close to the tensile strength may happen. If tensile failure happens, the internal friction angle will have no effect on the failure process; if shear failure happens close to the tensile yield criterion, the yield strength should be insensitive to the variation of the internal friction angle. In both scenarios, the internal friction angle should not dominate the thermally induced

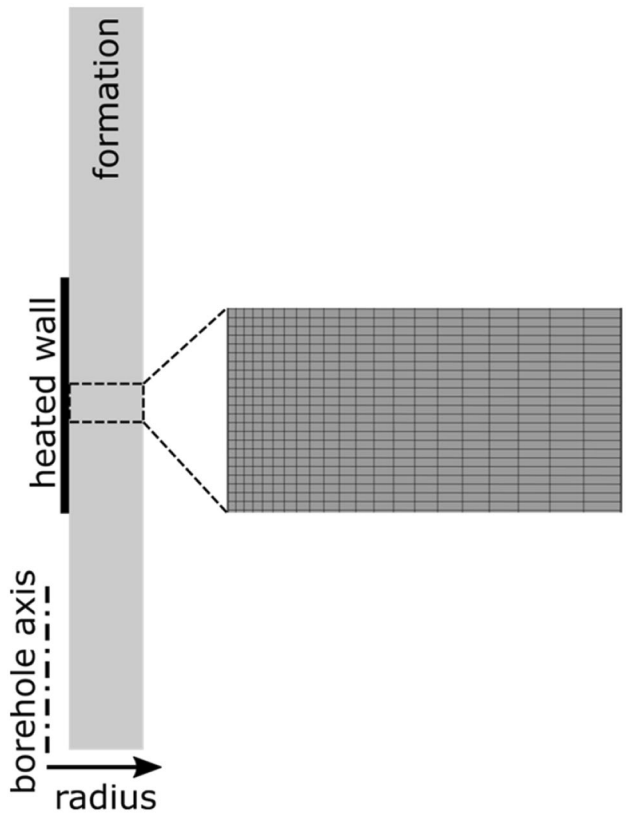

Fig. 21 The axisymmetric geometry of the field-scale simulation and the meshes

failure around the borehole. Figure 25 shows the parametric analysis of the internal friction angle based on the 1st field-shale test with the field-scale geometry, which proves the aforementioned analysis that the internal friction angle only contributes a limited amount to the borehole displacement. It is worth to notice that the observed small dependence on the internal friction angle is reasonable: as the friction angle decreases, the plastic region expands, which indicates enhanced plastic strain around the borehole.

A parametric analysis was carried out for the dilation angle, another critical parameter in the Mohr–Coulomb yield criterion. Figure 26 reveals that the borehole displacement is also not very sensitive to the dilation angle. We ascribe this result to the same reason as for the internal friction angle: tensile failure rather than shear failure dominates the borehole failure. In Fig. 26, it is seen that a higher dilation angle results in a lower borehole displacement, which can be explained in the following way: the dilation angle gives the ratio of the plastic volumetric strain to the plastic shear strain (Vermeer and de Borst 1984). A larger dilation angle implies a larger volumetric expansion of the rock resulting in an increase of pore volume (or permeability) and thus a decrease of pore pressure (enhanced drainage), which counteracts the increase of thermally induced pore-pressure and prevents rock failure in a further step. The result is less displacement at the borehole.

In the following, the impact of permeability will be discussed. The permeability applied in the simulation of the 1st field-shale was 300 nD, higher than the permeability (90 or 120 nD) used in the simulations of the 2nd field-shale test. Possibly during the consolidation stage of

Fig. 22 Simulation of field-scale borehole closure for heating of the borehole wall to 250 °C based on rock properties obtained from the 1st and the 2nd field-shale test

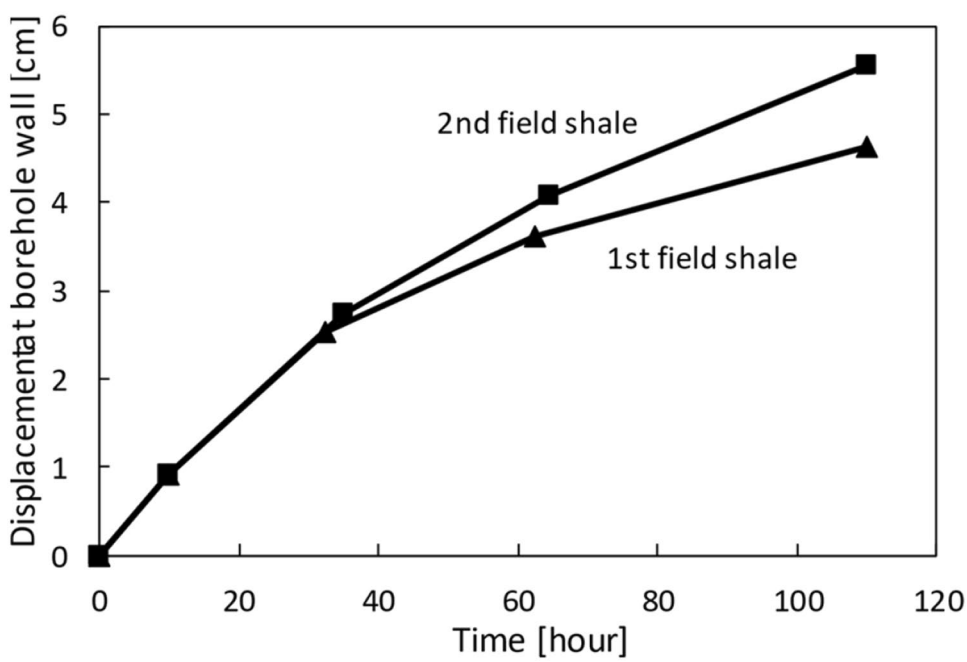

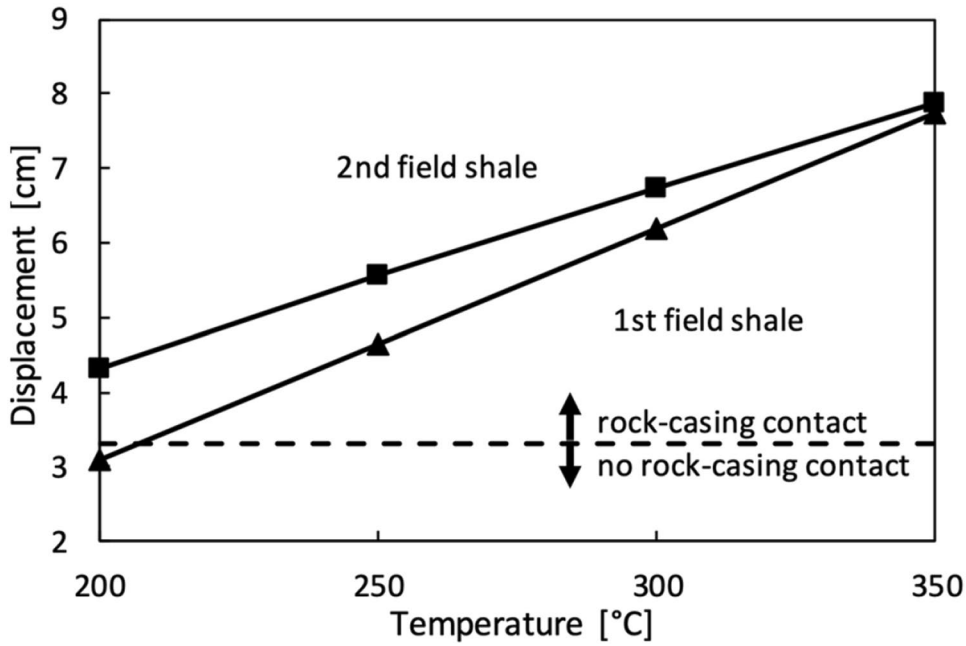

Fig. 23 Displacement at the borehole after 110-h heating at different temperatures

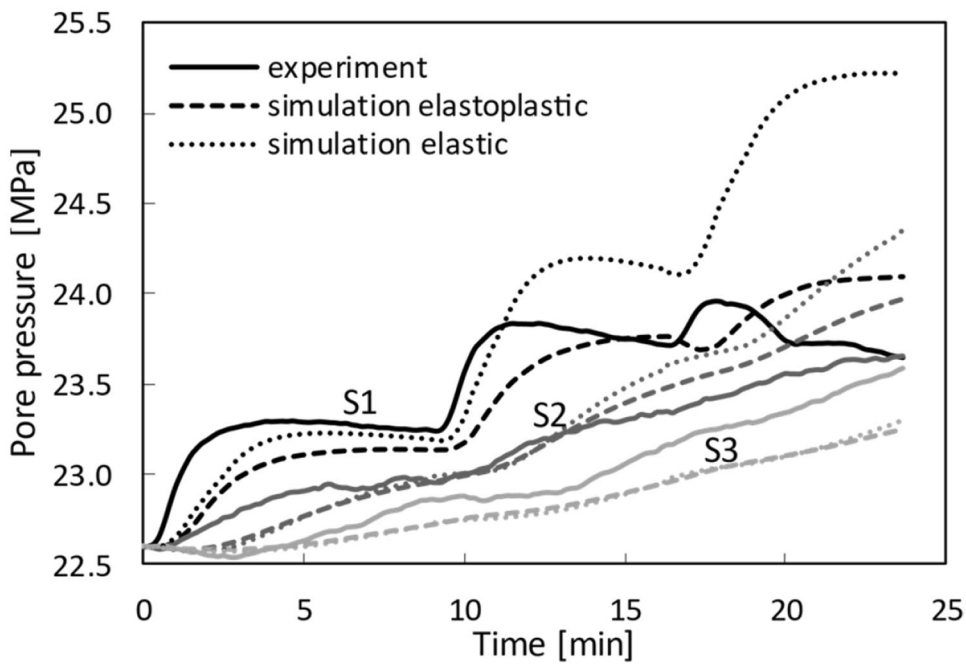

Fig. 24 Pore pressure time-evolution in elastic rock behavior based on the 1st field-shale. Solid-experiment; dash-simulation; dot-simulation elastic

the 1st field-shale test, the permeability around the borehole was enhanced due to the rock failure, triggered by an unforeseen pump stop resulting in a decrease of the borehole pressure (see Fig. 6). In the 2nd test of the field-shale, a similar event was avoided. Due to the dilatancy of the rock failure around the borehole, the porosity is expected to increase, which will, in turn, enhance the permeability of the rock (for example Collins 1976 and Costa 2006). In addition, the formation of cracks during rock failure results in a permeability increase. However, the numerical model used for the present simulations did not allow for a variable permeability that would depend on rock failure. To observe the effect of permeability, in the simulation of the 2nd field-shale test, we tried to match the pore pressure at S1 with two constant permeabilities, 90 nD and 120 nD. The simulation with 90 nD matches the first and the second heating sequence better, and the simulation with 120 nD matches the third heating sequence better (see Fig. 20). This indicates that the permeability increased during the third heating sequence, which agrees

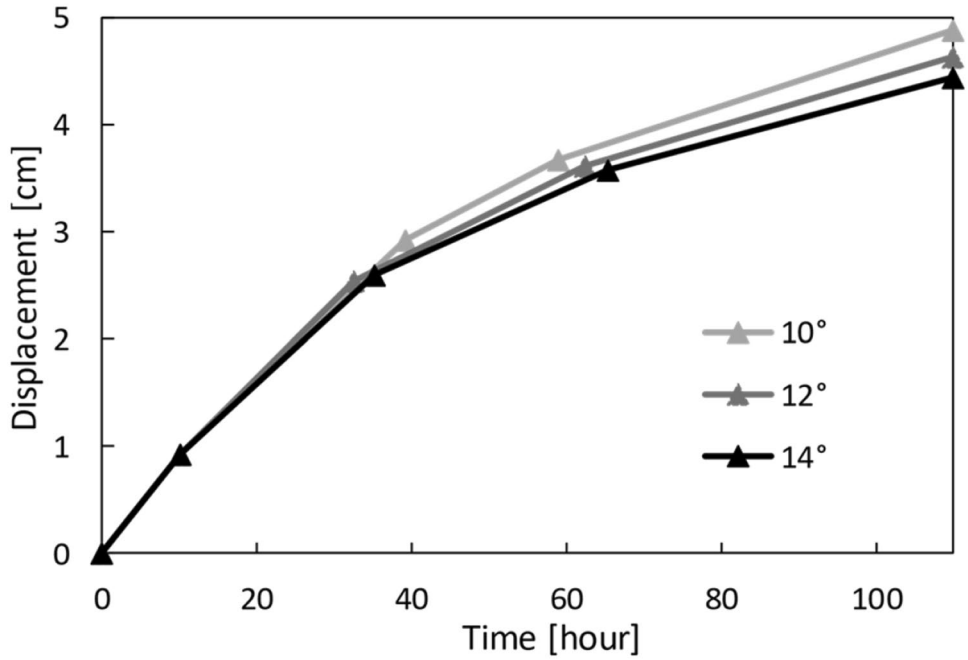

Fig. 25 Borehole displacement with different internal friction angles based on the 1st field-shale with the field-geometry (heating up to 250 °C in 10 h and holding for 100 h)

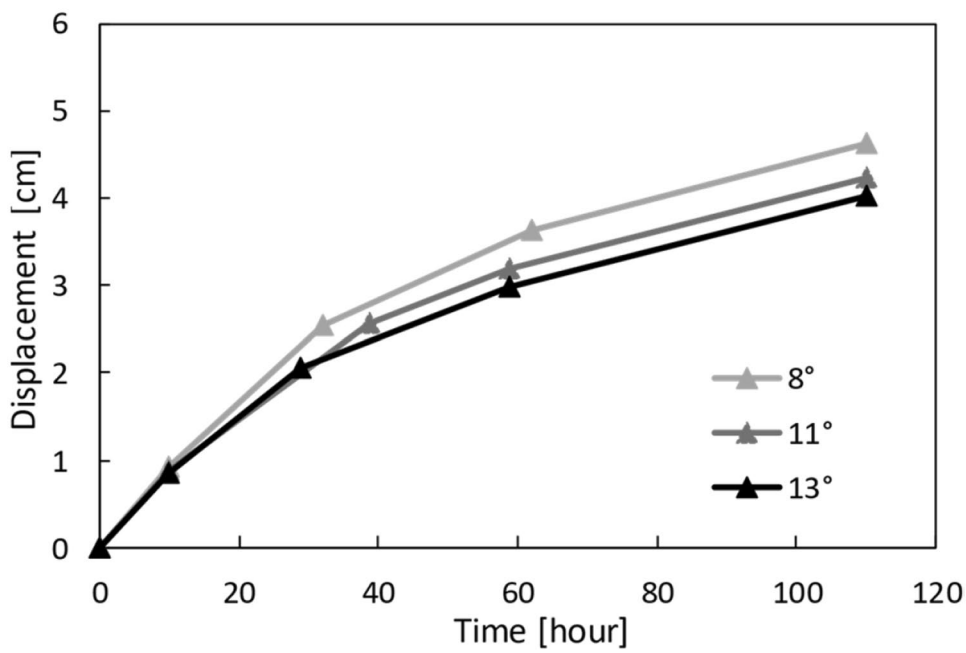

Fig. 26 Borehole displacement with different dilation angles based on the 1st field-shale parameter with field-geometry (heating up to 250 °C in 10 h and holding for 100 h)

with the explanation that rock failure and plasticity result in a permeability increase.

Figure 27 shows the simulation of the thermally induced borehole deformation with different permeabilities (90 nD, 300 nD, and 9000 nD). By only comparing the results for 90 nD and 300 nD, it is seen that lower permeability results in enhanced borehole-wall displacements at low target temperatures (in this example lower than 230 °C), which agrees with our expectation: lower permeability implies high thermal pressurization near the borehole that can contribute to rock failure. Surprisingly when the target temperature is higher than 230 °C, high permeability is more beneficial for borehole closure. We explain this observation as follows: a higher permeability can enhance the thermally induced pore-pressure diffusion resulting in a larger thermal-affected area around the borehole. When the heating temperature is high enough, the thermal pressurization will result in plastic yield in this enlarged area (not only the rock very close to the borehole), which in turn contributes to more borehole closure. However, if the permeability is too high borehole

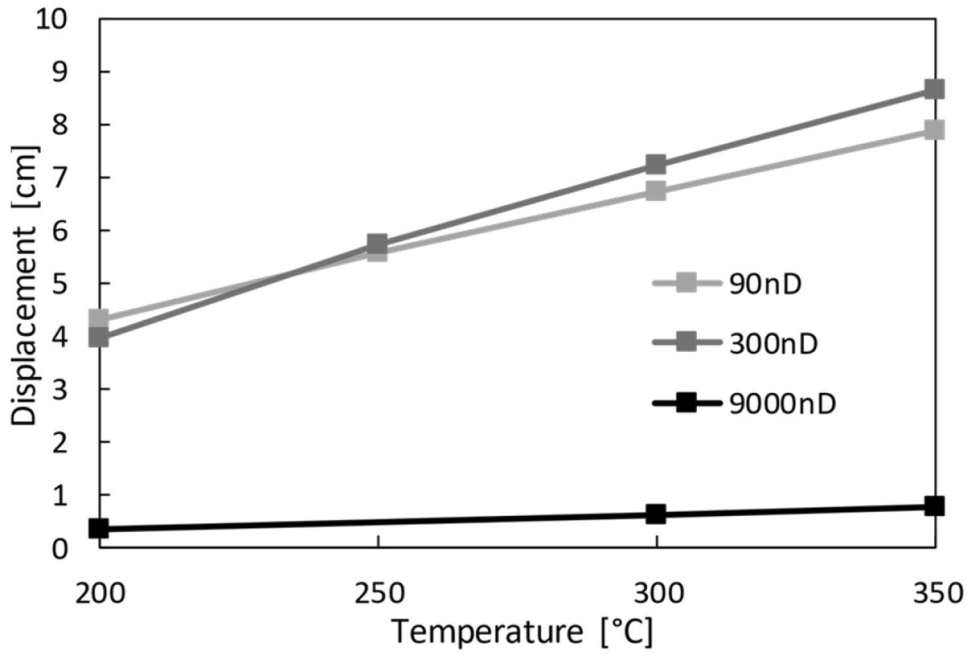

Fig. 27 Large-time (110 h) displacement at the borehole with permeability 90 nD, 300 nD, and 9000 nD

closure is impossible as seen in the simulation with 9000 nD in Fig. 27: the pore pressure reaches equilibrium quickly and almost no thermally induced failure happens.

In addition to permeabilities, Young's moduli were different in the two field-shale simulations. Young's modulus of the field-shale (0.13 GPa) is evaluated from Hooke's law based on an undrained loading–unloading triaxial test. The rock specimen is assumed to be isotropic (while it is actually anisotropic), so the evaluation contains an uncertainty. In the simulation of the 2nd field-shale, Young's modulus is increased to 0.53 GPa after several trials, which can lead to a better time-evolution of the pore pressure. The sensitivity analysis reveals a clear dependence of borehole closure on Young's modulus: as seen in Fig. 28, based on the 1st field-shale test, a lower Young's modulus (softer rock) results in larger borehole-wall displacement within the temperature range 200–350 °C. Based on the 2nd field-shale test, we obtain a similar conclusion as in the 1st test. However,

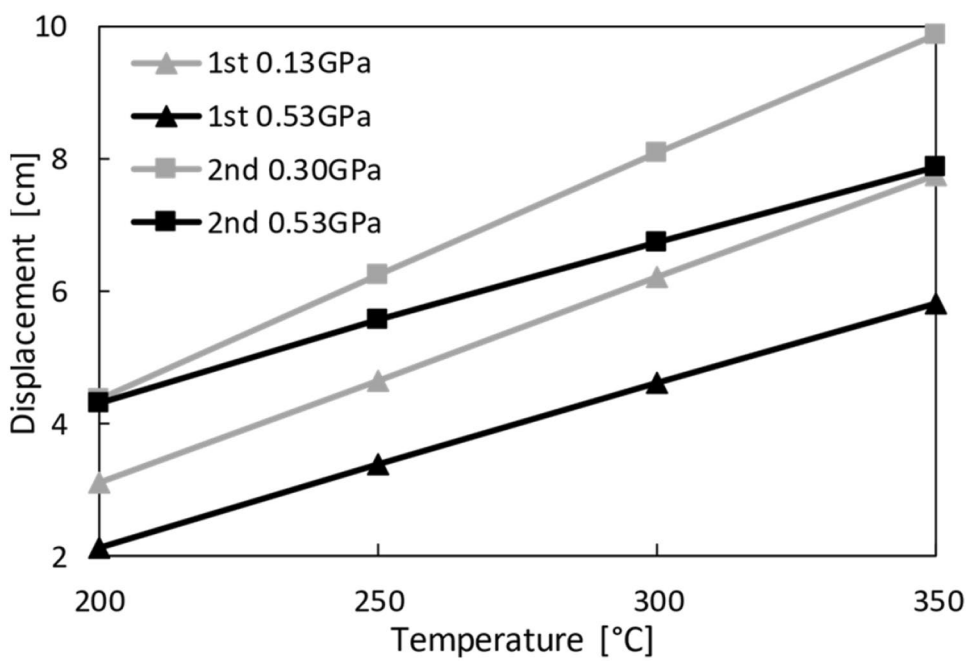

Fig. 28 Displacement at the borehole wall after 110 h with different Young's moduli based on both field-shale tests (For the 2nd field-shale, the simulation with Young's modulus 0.13 GPa is difficult to converge, so is substituted by 0.3 GPa, which does not affect the conclusion qualitatively)

when the heating temperature is below 200 °C, a higher Young's modulus (stiffer rock) results in a larger borehole-wall displacement.

Young's modulus can contribute to the borehole closure by two mechanisms. (i) Through Hooke's law, the higher Young's modulus indicates smaller rock deformation for the same stress change. (ii) Through the thermal stress, the higher Young's modulus results in a larger Mohr circle (shear stress concentration) while the formation around the borehole is heated (see the explanation of thermal stress in Sect. 1). The enlarged Mohr circle indicates a higher potential for shear failure. We observe that the influence of Young's modulus via these two mechanisms are the opposite. Below or above a specific temperature (200 °C based on the 2nd test), one of the mechanisms contributes more than the other.

For the 1st field-shale, the initial shear stress around the borehole is less than that of the 2nd field-shale. Thus when the borehole-wall is heated, it is possible that the tensile failure rather than the shear failure dominates the failure process (Figs. 25, 26 show that shear failure also contributes to the borehole closure but with limited contribution). Therefore, even though the increase of Young's modulus enhances the shear stress around the borehole, it only results in the limited shear failure close to the borehole. Consequently, higher Young's modulus results in less borehole closure through Hooke's law.

For the 2nd field-shale, the initial shear stress around the borehole is larger, which enhances shear failure especially with the thermal-induced shear stress. Both simulations with a stiff and soft rock in the 2nd field-shale show a larger borehole closure than that based on the 1st field-shale. It even can be expected that when the heating temperature is lower than 200 °C, the borehole closure with stiff rock is larger than that with soft rock, which indicates that higher Young's modulus results in more borehole closure through the thermal stress.

A cross-comparison of stiff rock based on both field-shales (either black or grey curves in Fig. 28) shows that shear stress/failure indeed enhances the borehole closure, and the impact of temperature is almost consistent with different states of shear stress.

Except for the specific discussions based on the lab tests and the simulations, several open questions will be addressed here as indications for the future work.

Two potential heating sources may be considered: (i) From production fluid during the life cycle of oil/gas production; ii. From a source provided on purpose as a part of P&A. In the first scenario, the production fluid takes the thermal energy from the reservoir and heats the shale rock at the shallower formation. This type of heating is very mild due to the limited temperature gradient and due to the dissipation of thermal energy during fluid transportation. The pore pressure in the shale can be in balance as it has enough time for diffusion. As a result, thermal pressurization will be limited to induce rock failure and heating efficiency can be a challenge. In the second scenario, an artificial heating tool can be run into the wellbore and heat the shale rock intensively. This heating source may be chemical-driven or electrical-driven. No matter in which way it is driven, the controllable artificial heating tool is a challenge. Very little information has been obtained in the literature review, which may call for in-depth research in the future.

The current study mainly focuses on how the thermal pressurization can induce borehole failure and hence trigger the borehole closure. If the displacement at the borehole wall is large enough to reach the casing, a rock-casing contact will be established (Xie et al. 2018). The formation of rock-casing contact should be studied further, as a weak contact may indicate that the rock-casing surface is a potential leakage path.

The rock is assumed as a plastic material in this study, which indicates that when the failure happens around the borehole the rock deformation happens instantaneously. In fact, the time-dependent borehole closure shown in Fig. 22 is due to diffusion rather than creep (the time-dependent deformation under a certain load) of the rock frame. Literature indicates the importance of shale creep (Chen and Small 2008; Sone and Zoback 2013; Lund and Kleiven 2016; Farhat et al. 2016, 2017; Nopola and Roberts 2016). Future work should focus on extending the elastoplastic rock model to a viscoelastic-plastic model (Liu et al. 2016; Shahsavari et al. 2016) or an elasto-viscoplastic one (Xie et al. 2019).

The current simulation uses perfect plasticity and is not able to tell the difference between brittle failure and ductile failure. Brittle failure observed in Pierre Shale has an adverse effect on the formation of shale barrier as brittle failure results in the formation of cracks that can provide hydraulic pathways resulting in an enhanced drainage area around the borehole and stabilize the pressure in the shale (a reduction of pore pressure moves the effective stress state away from the failure envelope). The field-shale used in this work is much softer, weaker and more ductile than the Pierre shale. Due to the ductile behavior, fewer cracks and fractures are created under failure so that thermal pressurization is maintained. Ductile shale is therefore a good candidate for the formation of thermally induced shale barrier.

A decrease of annulus pressure can trigger borehole closure due to shear stress concentration around the borehole (Fjær et al. 2008, 2018). In this study, we kept the borehole pressure constant. As an extension for both lab tests and simulations, the borehole pressure can be dropped to a lower level before or during heating, so the stress concentration can be enhanced, which in principle can induce more plastic deformation around the borehole.

6 Conclusion

This study aims to reveal whether heating can induce borehole closure. In low-permeability rocks, thermal diffusion is faster than pore-pressure diffusion. As a result, the pore pressure increases in the rock around the borehole during borehole heating, bringing the rock to shear or tensile failure. If the plastic deformations are large enough, the annulus between rock and casing can close.

In total, three samples, one Pierre-shale sample, and two field-shale samples from the North Sea, were tested in the lab. Before and after the test, CT images of the samples were obtained. During the test, temperatures, pore pressures, and strains were recorded. The CT images and the time-evolution of the pore pressures indicate that heating can result in rock failure around the borehole and to a various extent in borehole closure. Communication tests through the casing annulus showed in one field-shale test a significantly reduced annulus permeability after heating, even though a full hydraulic barrier was not established. Borehole failure also enhances the drainage in the rock due to the dilatancy and crack-formation.

The simulations focused on matching the stepwise-heating sequences in the tests. The Mohr–Coulomb failure criterion with tensile strength was applied in the simulations. Overall, the simulated temperatures match the experimental data very well, but matching the experimental pore pressure data was more challenging: a good match was achieved at all three sensors for the Pierre-shale but only for the innermost sensor for the field-shale tests with large discrepancies for the two other sensor data. The lab-scale simulations of the field-shale tests give indications for enhanced drainage caused by the thermally induced failure around the borehole. The field-scale simulations indicated that heating the borehole wall to a temperature above 220 °C and holding it for 100 h will result in a rock-casing contact. Note that the rock-casing contact does not mean that a hydraulic barrier is established. A parametric analysis indicated both tensile and shear failure can happen around the borehole; tensile failure occurs especially if shear stresses around the borehole are low.

The present study gives evidence that borehole heating can result in annulus closure which is a necessary condition for the formation of a hydraulic barrier. This suggests that borehole heating may potentially be considered as a novel substitution for conventional P&A operations.

Acknowledgements This work was sponsored by the Research Council of Norway, Aker BP, BP, ConocoPhillips, Equinor, Petrobras, Shell, and Total, through the PETROMAKS2 KPN-project: Shale Barrier Toolbox: Designing future wells for efficient completion and simpler P&A (Grant no. 280650/E30), by the Research Council of Norway, Aker BP, BP, ConocoPhillips, Equinor, Shell, and Total, through the PETROMAKS 2 KPN-project: Shale as a Permanent Barrier after Well Abandonment (Grant no. 244420/E30), and by AkerBP through the commercial project (Grant no. IK7021151).

Funding Open Access funding provided by SINTEF AS.

Compliance with Ethical Standards

Conflict of interest The authors declare that they have no conflict of interest.

Open Access This article is licensed under a Creative Commons Attribution 4.0 International License, which permits use, sharing, adaptation, distribution and reproduction in any medium or format, as long as you give appropriate credit to the original author(s) and the source, provide a link to the Creative Commons licence, and indicate if changes were made. The images or other third party material in this article are included in the article's Creative Commons licence, unless indicated otherwise in a credit line to the material. If material is not included in the article's Creative Commons licence and your intended use is not permitted by statutory regulation or exceeds the permitted use, you will need to obtain permission directly from the copyright holder. To view a copy of this licence, visit http://creativecommons.org/licenses/by/4.0/.

References

Abousleiman Y, Ekbote S (2005) Solutions for the inclined borehole in a porothermoelastic transversely isotropic medium. J Appl Mech 72:102–114. https://doi.org/10.1115/1.1825433

Batzle M, Wang Z (1992) Seismic properties of pore fluids. Geophysics 57:1396–1408. https://doi.org/10.1190/1.1443207

Bauer A, Stenebråten JF, Li L, Fjær E (2017) Can heating-induced creep result in shale barriers for P&A applications? In: 51st U.S. Rock mechanics/geomechanics symposium proceedings. American Rock Mechanics Association

Bauer A, Xie X, Stenebråten JF, et al (2019) Heating induced shale barriers. In: Sixth EAGE shale workshop proceedings

Bear J, Corapcioglu MY (1981) A mathematical model for consolidation in a thermoelastic aquifer due to hot water injection or pumping. Water Resour Res 17:723–736. https://doi.org/10.1029/WR017i003p00723

Biot MA (1941) General theory of three-dimensional consolidation. J Appl Phys 12:155–164. https://doi.org/10.1063/1.1712886

Biot MA (1955) Theory of elasticity and consolidation for a porous anisotropic solid. J Appl Phys 26:182–185

Biot MA (1956) Thermoelasticity and irreversible thermodynamics. J Appl Phys 27:240–253. https://doi.org/10.1063/1.1722351

Campanella RG, Mitchell JK (1968) Influence of temperature variations on soil behavior. J Soil Mech Found Div

Chen G, Ewy RT (2005) Thermoporoelastic effect on wellbore stability. SPE J 10:121–129. https://doi.org/10.2118/89039-PA

Chen R, Small JC (2008) Analysis of the creep behaviour of tunnels in sandstone/shale. In: 13th Australian Tunnelling Conference. Australasian Institute of Mining and Metallurgy. https://www.scopus.com/record/display.uri?eid=2-s2.0-58049186372&origin=inward&txGid=5ea45e3c7af7543333557d3c21b65dee

Collins RE (1976) Flow of fluids through porous materials. Petroleum Publishing Co.,Tulsa, OK, United States. https://www.osti.gov/biblio/7099752

Costa A (2006) Permeability-porosity relationship: a reexamination of the Kozeny-Carman equation based on a fractal

pore-space geometry assumption. Geophys Res Lett. https://doi.org/10.1029/2005GL025134
Coussy O (1989) A general theory of thermoporoelastoplasticity for saturated porous materials. Transp Porous Media. https://doi.org/10.1007/BF00138040
Coussy O (1995) Mechanics of porous continua. Wiley, Chichester
Cryer CWA (1963) A comparison of the three-dimensional consolidation theories of Biot and Terzaghi. Q J Mech Appl Math 16:401–412
Cui L, Cheng AH-D, Abousleiman Y (1997) Poroelastic solution for an inclined borehole. J Appl Mech 64:32–38. https://doi.org/10.1115/1.2787291
Dassault Systèmes (2014) Abaqus Analysis User's Guide
Delage P (2013) On the thermal impact on the excavation damaged zone around deep radioactive waste disposal. J Rock Mech Geotechn Eng 5:179–190. https://doi.org/10.1016/j.jrmge.2013.04.002
Detournay E, Cheng AH-D (1988) Poroelastic response of a borehole in a non-hydrostatic stress field. Int J Rock Mech Min Sci Geomech Abstr 25:171–182. https://doi.org/10.1016/0148-9062(88)92299-1
Farhat F, Shen WQ, Shao JF, et al (2016) Multi-scale modeling of time-dependent behavior of claystones. American Rock Mechanics Association, ARMA
Farhat F, Shen WQ, Shao JF (2017) A micro-mechanics based viscoplastic model for clayey rocks. Comput Geotech 89:92–102. https://doi.org/10.1016/j.compgeo.2017.04.014
Favero V (2017) Multiphysical behaviour of shales from Northern Switzerland. In: Infoscience. https://infoscience.epfl.ch/record/225966. Accessed 24 Jun 2019
Fjær E, Holt RM, Raaen A et al (2008) Petroleum related rock mechanics, 2nd edn. Elsevier, Amsterdam
Fjær E, Stenebråten JF, Bakheim S (2018) Laboratory test for studies on shale barrier formation. In: 52nd U.S. Rock mechanics/geomechanics symposium proceedings. American Rock Mechanics Association
Gao J, Deng J, Lan K et al (2017) Porothermoelastic effect on wellbore stability in transversely isotropic medium subjected to local thermal non-equilibrium. Int J Rock Mech Min Sci 96:66–84. https://doi.org/10.1016/j.ijrmms.2016.12.007
Ghabezloo S, Sulem J (2009) Stress dependent thermal pressurization of a fluid-saturated rock. Rock Mech Rock Eng 42:1–24. https://doi.org/10.1007/s00603-008-0165-z
Ghabezloo S, Sulem J (2010) Effect of the volume of the drainage system on the measurement of undrained thermo-poro-elastic parameters. Int J Rock Mech Min Sci 47:60–68
Haddad M, Eichhubl P (2020) Poroelastic models for fault reactivation in response to concurrent injection and production in stacked reservoirs. Geomech Energy Environ 24:100181. https://doi.org/10.1016/j.gete.2020.100181
Haug C (2019) Numerical modelling of production-induced stress changes and seismicity in fault-compartmentalized reservoirs of the North German Basin. PhD Thesis, Technische Universität
Hojka K, Dusseault MB (1990) An analytical solution for the steady-state temperature and stress fields around a borehole during fluid injection. SPE-21632-MS 40. https://www.onepetro.org/general/SPE-21632-MS
Hou Z, Luo X (2011) Investigation of thermal effect on stability of deep wellbores in low and high permeable formations. In: 12th ISRM congress proceedings. International Society for Rock Mechanics and Rock Engineering
Hueckel T, Borsetto M (1990) Thermoplasticity of saturated soils and shales: constitutive equations. J Geotech Eng 116:1765–1777. https://doi.org/10.1061/(ASCE)0733-9410(1990)116:12(1765)
Johnston D (1987) Physical properties of shale at temperature and pressure. Geophysics 52:1391–1401. https://doi.org/10.1190/1.1442251
Kanfar MF, Chen Z, Rahman SS (2015) Effect of material anisotropy on time-dependent wellbore stability. Int J Rock Mech Min Sci 78:36–45. https://doi.org/10.1016/j.ijrmms.2015.04.024
Kanfar MF, Chen Z, Rahman SS (2016) Fully coupled 3D anisotropic conductive-convective porothermoelasticity modeling for inclined boreholes. Geothermics 61:135–148. https://doi.org/10.1016/j.geothermics.2016.01.010
Kurashige M (1989) A thermoelastic theory of fluid-filled porous materials. Int J Solids Struct 25:1039–1052. https://doi.org/10.1016/0020-7683(89)90020-6
Li X (1998) Thermoporomechanical modelling of inclined boreholes. Thesis
Liu C, Zhou F, Kang J, Xia T (2016) Application of a non-linear viscoelastic-plastic rheological model of soft coal on borehole stability. J Natur Gas Sci Eng 36(1):1303–1311. https://www.sciencedirect.com/science/article/pii/S1875510016301329
Lund E, Kleiven ML (2016) Creep and Consolidation in Pierre Shale-Identification of how time-dependent effects are influenced by alteration in pore fluid pH and changes in stress conditions. Master's Thesis, Norwegian University of Science and Technology. https://ntnuopen.ntnu.no/ntnu-xmlui/handle/11250/2402909?show=full
Mandel J (1953) Consolidation des sols (étude mathématique). Geotechnique 3:287–299
McTigue DF (1986) Thermoelastic response of fluid-saturated porous rock. J Geophys Res Solid Earth 91:9533–9542
McTigue DF (1990) Flow to a heated borehole in porous, thermoelastic rock: analysis. Water Resour Res 26:1763–1774. https://doi.org/10.1029/WR026i008p01763
Mohajerani M, Delage P, Sulem J, et al (2013) A laboratory investigation of thermally induced pore pressures in the Callovo-Oxfordian Claystone. arXiv:13035304 (physics)
Nayar KG, Sharqawy MH, Banchik LD, Lienhard VJH (2016) Thermophysical properties of seawater: a review and new correlations that include pressure dependence. Desalination 390:1–24. https://doi.org/10.1016/j.desal.2016.02.024
Nopola JR, Roberts LA (2016) Time-dependent deformation of pierre shale as determined by long-duration creep tests. American Rock Mechanics Association, ARMA
Norsok D (2013) Well integrity in drilling and well operations. NOSOK D-010 Rev 4. https://www.standard.no/GLOBAL/PDF/PETROLEUM/D-010%20MINI%20ENQUIRY/9.%20PLUG%20AND%20ABANDONMENT%20(15.8.12)_REVISJON%20TIL%20EKSISTERENDE.PDF
Palciauskas VV, Domenico PA (1982) Characterization of drained and undrained response of thermally loaded repository rocks. Water Resour Res 18:281–290. https://doi.org/10.1029/WR018i002p00281
Rice JR (1975) On the stability of dilatant hardening for saturated rock masses. J Geophys Res 80:1531–1536. https://doi.org/10.1029/JB080i011p01531
Rice JR, Cleary MP (1976) Some basic stress diffusion solutions for fluid-saturated elastic porous media with compressible constituents. Rev Geophys 14:227–241. https://doi.org/10.1029/RG014i002p00227
Robertson EC (1988) Thermal Properties of Rocks. United States Department of the Interior Geological Survey, Restion
Salisbury DP, Ramos GG, Wilton BS (1991) Wellbore instability of shales using a downhole simulation test cell. In: The 32nd U.S. symposium on rock mechanics (USRMS) proceedings. American Rock Mechanics Association
Shahsavari H, Naghdabadi R, Baghani M, Sohrabpour S (2016) A finite deformation viscoelastic–viscoplastic constitutive model for self-healing materials. Smart Mater Struct 25:125027

Sharqawy MH, Lienhard JH, Zubair SM (2010) Thermophysical properties of seawater: a review of existing correlations and data. Desalin Water Treat 16:354–380. https://doi.org/10.5004/dwt.2010.1079

Sone H, Zoback MD (2013) Mechanical properties of shale-gas reservoir rocks—Part 2: ductile creep, brittle strength, and their relation to the elastic modulus. Geophysics 78:D393–D402

Stephens G, Voight B (1982) Hydraulic fracturing theory for conditions of thermal stress. Int J Rock Mech Min Sci Geomech Abs 19:279–284. https://doi.org/10.1016/0148-9062(82)91364-X

Uribe-Patiño JA, Alzate-Espinosa GA, Arbeláez-Londoño A (2017) Geomechanical aspects of reservoir thermal alteration: a literature review. J Petrol Sci Eng 152:250–266. https://doi.org/10.1016/j.petrol.2017.03.012

Vermeer PA, de Borst R (1984) Non-associated plasticity for soils, concrete and rock. HERON 29(3):1984

Walsh JB (1973) Theoretical bounds for thermal expansion, specific heat, and strain energy due to internal stress. J Geophys Res 1896–1977(78):7637–7646. https://doi.org/10.1029/JB078i032p07637

Wang Y, Dusseault MB (1995) Response of a circular opening in a friable low-permeability medium to temperature and pore pressure changes. Int J Numer Anal Meth Geomech 19:157–179. https://doi.org/10.1002/nag.1610190302

Wang Y, Papamichos E (1994) Conductive heat flow and thermally induced fluid flow around a well bore in a poroelastic medium. Water Resour Res 30:3375–3384. https://doi.org/10.1029/94WR01774

Wang Y, Papamichos E, Dusseault MB (1996) Thermal stresses and borehole stability. In: 2nd North American Rock Mechanics Symposium Proceedings. American Rock Mechanics Association

Williams S, Carlsen T, Constable K, Guldahl A (2009) Identification and qualification of shale annular barriers using wireline logs during plug and abandonment operations. In: SPE/IADC drilling conference, Proceedings. pp 342–356

Xie X, Detournay E, Fjaer E (2018) The build-up of contact pressure behind casing due to formation creep. In: 52nd US Rock mechanics/geomechanics symposium proceedings

Xie X, Fjaer E, Detournay E (2019) Time-dependent closure of a borehole in a viscoplastic rock. Geomech Energy Environ. https://doi.org/10.1016/j.gete.2019.02.001

Yan C, Deng J, Yu B et al (2014) Borehole stability in high-temperature formations. Rock Mech Rock Eng 47:2199–2209. https://doi.org/10.1007/s00603-013-0496-2

Yao B, Wang L, Yin X, Wu Y-S (2017) Numerical modeling of cryogenic fracturing process on laboratory-scale Niobrara shale samples. J Natur Gas Sci Eng 48:169–177. https://doi.org/10.1016/j.jngse.2016.10.041

Yu L, Weetjens E, Sillen X et al (2014) Consequences of the thermal transient on the evolution of the damaged zone around a repository for heat-emitting high-level radioactive waste in a clay formation: a performance assessment perspective. Rock Mech Rock Eng 47:3–19. https://doi.org/10.1007/s00603-013-0409-4

Zeuch DH (1983) The mechanical behavior of Anvil Points oil shale at elevated temperatures and confining pressures. Can Geotech J 20:344–352. https://doi.org/10.1139/t83-037

Publisher's Note Springer Nature remains neutral with regard to jurisdictional claims in published maps and institutional affiliations.